

NASA TECHNICAL NOTE



NASA TN D-6103

C.1

NASA TN D-6103

LOAN COPY: RET
AFWL (DOG
KIRTLAND AFB

0133283



TECH LIBRARY KAFB, NM

FLOW FIELD RESULTING FROM
FORWARD-FACING NOZZLES EXHAUSTING
NEAR A LARGE CYLINDRICAL BODY
AT FREE-STREAM MACH NUMBERS
OF 3.0, 4.5, AND 6.0

by James A. Martin and Robert J. McGhee

Langley Research Center

Hampton, Va. 23365

NATIONAL AERONAUTICS AND SPACE ADMINISTRATION • WASHINGTON, D. C. • JANUARY 1971



0133283

1. Report No. NASA TN D-6103		2. Government Accession No.		3. Recipient's Catalog No.	
4. Title and Subtitle FLOW FIELD RESULTING FROM FORWARD-FACING NOZZLES EXHAUSTING NEAR A LARGE CYLINDRICAL BODY AT FREE-STREAM MACH NUMBERS OF 3.0, 4.5, AND 6.0				5. Report Date January 1971	
				6. Performing Organization Code	
7. Author(s) James A. Martin and Robert J. McGhee				8. Performing Organization Report No. L-7333	
				10. Work Unit No. 126-13-10-22	
9. Performing Organization Name and Address NASA Langley Research Center Hampton, Va. 23365				11. Contract or Grant No.	
				13. Type of Report and Period Covered Technical Note	
12. Sponsoring Agency Name and Address National Aeronautics and Space Administration Washington, D.C. 20546				14. Sponsoring Agency Code	
15. Supplementary Notes					
16. Abstract Effects of nozzles exhausting forward near a large cylindrical body have been investigated for free-stream Mach numbers of 3.0, 4.5, and 6.0 and Reynolds numbers per meter (foot) from 2.6×10^6 (0.8×10^6) to 6.6×10^6 (2.0×10^6). Jet pressure, forebody shape, centerbody length, number of nozzles firing, and jet Mach number were varied. The extent of the nozzle-exhaust flow was constrained by the location of the bow shock wave. Free-interaction transitional and turbulent separation existed as well as separation at the forebody-cylinder juncture. Jet stagnation pressure, jet static pressure, and jet mass flow appeared to be the dominant nozzle parameters.					
17. Key Words (Suggested by Author(s)) Exhaust plumes Separated flow Launch vehicles				18. Distribution Statement Unclassified - Unlimited	
19. Security Classif. (of this report) Unclassified		20. Security Classif. (of this page) Unclassified		21. No. of Pages 59	
				22. Price* \$3.00	

FLOW FIELD RESULTING FROM FORWARD-FACING NOZZLES
EXHAUSTING NEAR A LARGE CYLINDRICAL BODY AT
FREE-STREAM MACH NUMBERS OF 3.0, 4.5, AND 6.0

By James A. Martin and Robert J. McGhee
Langley Research Center

SUMMARY

Some effects of forward-facing supersonic conical nozzles exhausting nitrogen into an oncoming stream near a large cylindrical body have been investigated for free-stream Mach numbers of 3.0, 4.5, and 6.0. Schlieren data and surface pressure data forward of one of the nozzles were obtained. The jet pressure was varied over a wide range at jet-exit Mach numbers from 2.20 to 4.60. The Reynolds number per meter (foot) varied from approximately 2.6×10^6 (0.8×10^6) to 6.6×10^6 (2.0×10^6). Forebody shape, centerbody length, and number of nozzles firing were also varied.

The investigation showed that the location of the bow shock wave was important in determining the extent of the flow which originates as the exhaust flow from the nozzles. When the flow which was initially the free-stream flow separated at the forebody-cylinder juncture, the level of the surface pressures was closely related to the separation angle. When the separation occurred on the cylindrical section of the model, it was free-interaction separation and both transitional and turbulent types appeared to exist, depending on local Reynolds number. Jet stagnation pressure, jet static pressure, and jet mass flow appeared to be the dominant nozzle parameters in determining the extent to which the flow from the nozzles affected the flow field. The surface pressure just forward of the nozzle exit did not depend on free-stream conditions and therefore was similar to static test results for underexpanded free jets impinging upon an adjacent surface, except for the smaller ratios of jet-exit static pressure to free-stream static pressure.

INTRODUCTION

During flights of rocket vehicles at high altitudes and high Mach numbers, the rocket-motor nozzles often exhaust at pressures far greater than the pressure of the surrounding environment. Exhaust plumes result which may cause extensive boundary-layer separation and high surface heating. If the jet exhaust impinges upon adjacent surfaces, large local loads may occur. Investigations of such problems have been reported, for example, in references 1 and 2.

When rocket-motor nozzles exhaust forward, such as when retrorockets are employed for separation of tandem vehicle stages, the resulting flow field, as shown in reference 3, can contain extensive regions of flow separation and can result in large local surface pressures. Because this complex flow field is difficult to analyze, an additional experimental investigation was initiated to further the understanding of the flow field which results when forward-facing supersonic nozzles are exhausted near a body immersed in a high supersonic or low hypersonic stream. The effects on the flow field and local surface pressures were investigated for variations in jet pressure, forebody shape, centerbody length, number of nozzles firing, and nozzle characteristics.

SYMBOLS

The data were obtained in the U.S. Customary Units but are presented in both International Units (SI) and U.S. Customary Units.

$C_{p,6}$ impingement pressure coefficient, $\frac{p_6 - p_j}{q_j}$

$(C_{p,6})_{\text{mod}}$ modified pressure coefficient, $\frac{\frac{p_6}{p_\infty} - \frac{p_j}{p_\infty}}{\frac{\gamma_j}{2} M_j^2 \frac{(T/T_t)_j}{\beta_j}}$

d diameter of cylinder, 6.71 cm (2.64 in.)

M_∞ free-stream Mach number

M_j jet-exit Mach number, calculated from ideal one-dimensional flow

p local surface static pressure

p_j jet-exit static pressure

$p_{t,j}$ jet stagnation pressure measured in plenum chamber

$\bar{p}_{t,j}$ ratio of jet stagnation pressure to reference jet stagnation pressure,
 $p_{t,j}/6.895 \text{ MN/m}^2 \left(p_{t,j}/1000 \text{ lb/in}^2 \right)$

p_6 static pressure at orifice 6 (see fig. 2)

p_{∞}	free-stream static pressure
q_j	jet dynamic pressure
$(T/T_t)_j$	ratio of static temperature to stagnation temperature of jet
x	orifice location measured from model base
$\beta_j = \sqrt{M_j^2 - 1}$	
γ_j	ratio of specific heats of jet ($\gamma_j = 1.40$)

APPARATUS AND TESTS

Model

A sketch of the general arrangement of the models is shown in figure 1, and model details are shown in figure 2. Each model consisted of a forebody, a centerbody, and an afterbody. The forebodies and centerbodies were constructed of aluminum. The afterbody was constructed of steel and housed the plenum chamber for the compressed gas supply to the four nozzles. The compressed gas passed through a hollow sting and was admitted into the plenum chamber through louvers, as in the investigation of reference 3. The 30° half-angle cone, 15° half-angle cone, ogive, and flat forebodies (fig. 2) were interchangeable with the short centerbody. (See fig. 1.) The 16° half-angle cone forebody and long centerbody (fig. 1) arrangement was the same model component used in the investigation of reference 3 and could be used only as a unit. A common afterbody was used for all test models.

Four different sets of conical nozzles (fig. 2) were used in the investigation and provided jet-exit Mach numbers of 2.20, 3.01, 3.68, and 4.60 which were calculated for gaseous nitrogen from one-dimensional theory. Caps were provided so that any combination of one to four nozzles could be tested. Gaseous nitrogen at local atmospheric temperature was the exhaust medium.

Wind Tunnel

The tests were conducted in a 0.6048-meter (2 foot) hypersonic facility at the Langley Research Center. This wind tunnel, described in reference 4, is an ejector type which provides continuous flow at high Mach numbers and low densities. The average test conditions are shown in the following table:

M_∞	Stagnation temperature		Stagnation pressure		Reynolds number	
	$^{\circ}\text{K}$	$^{\circ}\text{R}$	kN/m^2	lb/ft^2	per meter	per foot
3.0	311	560	96	2005	6.56×10^6	2.0×10^6
4.5	422	760	115	2402	2.62	.80
6.0	422	760	310	6474	3.28	1.0

Nitrogen Supply

High-pressure gaseous nitrogen was generated by pumping liquid nitrogen to the required storage pressure and converting it from liquid to gas in a steam-actuated heat exchanger. The high-pressure gaseous nitrogen was then stored in tanks with a capacity of 22.65 m^3 (800 ft^3). Suitable pressure-reducing and pressure-regulating valves were remotely controlled to obtain the nitrogen gas pressure in a manifold outside the test section which, in turn, fed the nozzle plenum chamber in the model. Once the correct pressure was obtained in the manifold, a quick-acting guillotine valve was employed to initiate and terminate the flow to the nozzles. Minor pressure adjustments could be made after initiation of flow through the nozzles.

Instrumentation

Six static pressure orifices 0.15 cm (0.06 in.) in diameter were located on the body surface in the plane of the model center line and nozzle 1 forward of the top-mounted nozzle as shown in figure 2. Simultaneous measurements of the six orifice pressures, as well as the nozzle plenum pressure, were obtained from absolute-pressure-measuring transducers. Data were obtained by a high-speed data acquisition system and recorded on magnetic tape. In addition, schlieren photographs taken at each datum point with the use of a 2-microsecond flash from a xenon light source were used for a visual study of the jet-interaction phenomena.

Tests and Accuracy

The models were tested at free-stream Mach numbers of 3.0, 4.5, and 6.0. The jet stagnation pressures were varied from 0.345 to 8.274 MN/m^2 (50 to 1200 lb/in^2). All data were obtained without boundary-layer trips on the model because no particular flight condition was simulated. At jet-off conditions, transitional flow probably existed over the rear of the long centerbody model for $M_\infty = 3.0$, but because of the low Reynolds numbers at $M_\infty = 4.5$ and $M_\infty = 6.0$, the flow was probably laminar over the entire model.

The free-stream Mach number in the region of the test model was accurate within ± 0.04 . The jet stagnation pressures quoted herein are estimated to be accurate within

± 2 percent. The jet Mach numbers were calculated from ideal one-dimensional inviscid flow and the measured throat and exit diameters of each nozzle. The nozzles were measured before and after the test and the variation in the calculated exit Mach number due to variations between nozzles and wear was determined to be 0.10 for the worst case. The effect of variations from ideal one-dimensional inviscid flow has not been determined. The absolute level of accuracy has not been established for the local surface static-pressure data, but the values of p/p_∞ presented are believed to give an accurate indication of the trends and levels of the surface pressure at that orifice. The pressure data at orifice 6 exhibited a nonrepeatability of about 25 percent. Approximately 20 seconds of time elapsed before each data point was taken.

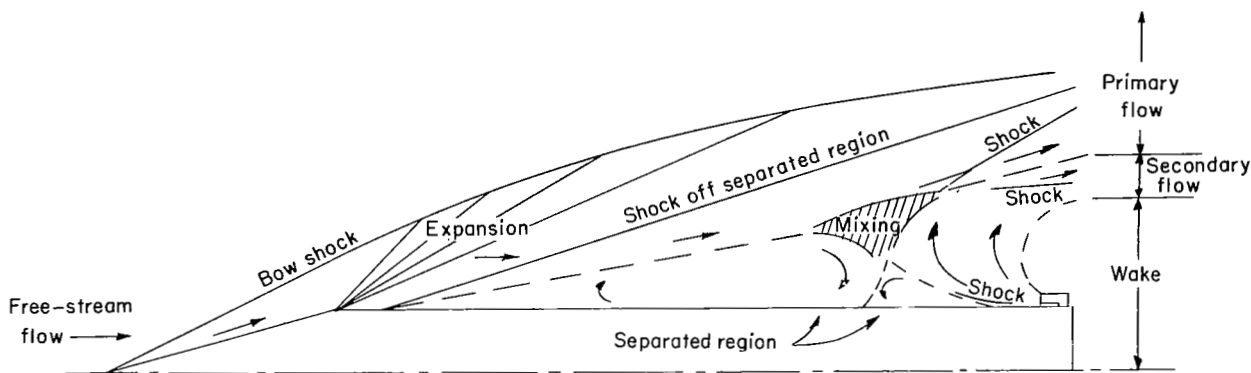
RESULTS AND DISCUSSION

The results of this investigation have been arranged to illustrate the flow field which results when forward-facing nozzles are exhausted near a body into an oncoming stream and the changes which occur in the flow field due to variations of jet pressure, model geometry, number of nozzles firing, and nozzle characteristics.

Figure 3 shows the flow field for the basic test condition around which parameters were varied at $M_\infty = 6.0$. The basic test condition consisted of the reference jet pressure ($p_{t,j} = 6.895 \text{ MN/m}^2$ or 1000 lb/in^2), the 30° cone forebody, and the short center-body with four $M_j = 3.68$ nozzles. Figures 4 to 17 illustrate the effect of parameter variations on the flow field. Jet-off data have been included for reference. Figures 18 to 20 show a correlation of jet-impingement pressure.

Basic Test Condition at $M_\infty = 6.0$

A schlieren photograph of the flow field for the basic test condition at $M_\infty = 6.0$ is shown in figure 3(a) and pertinent details have been identified in the schematic representation of this flow field presented in figure 3(b). There are four portions of the flow field: the primary flow (initially the free stream); the secondary flow (originating as the exhaust flow from the nozzles and turning outward and rearward); a viscosity-induced portion (bounded by the primary and secondary flows and the body); and the wake (behind the body and the secondary flow). Detailed descriptions of these portions of the flow field have been given in reference 3 and the flow field is indicated in sketch (a). Some disturbances from the secondary flows from nozzles 2 and 4, on the sides of the model, are visible in figures 3(a) and 3(b) but are located out of the plane of the model center line and nozzle 1. All other features referred to in the photographs are essentially located in the plane of the model center line and nozzle 1.



Sketch (a).-- Schematic representation of flow-field model.

The location of the primary separation streamline (between the primary flow and the forward section of the separated region) is clearly defined where the shear layer is laminar (near the separation point, which is shown for this test condition at the cone-cylinder juncture) but is poorly defined from shear-layer transition to the confluence of the shear layers (where the primary and secondary shear layers join). A shear layer is presumed to be laminar if it appears as a thin white line and turbulent if it appears as a wide uneven band. The location of the secondary flow separation streamline (between the secondary flow and the aft section of the separated region) is likewise clearly defined until transition occurs in the shear layer and then poorly defined to the confluence region. The separation of the secondary flow is of the free-interaction type. ("Free interaction" is the term used to describe separation which occurs without a local constraint on the location of the separation point other than interaction of the boundary layer and the inviscid flow external to the boundary layer.) The primary flow inside the bow shock wave, as shown, seems to divide, leave the plane of the model center line and nozzle 1, and flow around the sides of the secondary flow; thus, the bow shock wave was allowed to intersect the boundary of the secondary flow. The bow shock wave is straight for a short distance behind the expansion but then turns outward where it is intersected first by compression waves from the thickening of the shear layer; second, by compression waves from the confluence of the shear layers; and finally, by the boundary of the secondary flow itself. A boundary between the secondary flow and the presumed wake is indicated on the schematic, but since this boundary was not discernible on the photograph its location is at best only approximate.

The pressure data for the basic test condition at $M_\infty = 6.0$ is shown in figure 6(c) ($\bar{p}_{t,j} = 1.0$). Because the separation point was at the cone-cylinder juncture, the pressure at even the forward orifices was higher than that for the jet-off condition. Orifices 1 and 2 were in the region of separated flow where the shear layer was laminar. Orifice 3 was in the region where the shear layers were turbulent and near the confluence

of the shear layers, and orifice 4 was near the station at which transition occurred in the shear layer of the secondary flow. Orifice 5 was under the laminar part of the secondary shear layer and therefore the pressure was lower. Orifice 6 was just forward of the jet impingement and therefore registered a high pressure.

Effect of Free-Stream Conditions

In figures 4 to 17, as M_∞ increased, free-stream static pressure and Reynolds number decreased. Because these additional changes both greatly affect the resulting flow field and surface pressure distribution, direct comparison of data at different free-stream Mach numbers cannot be made in most figures. The free-stream Mach number directly affects the position of the bow shock wave. The importance of the bow-shock-wave location is discussed when the effect of forebody shape is presented.

Where free-interaction separation occurred, the shear layer was transitional or turbulent, depending at least partly on the free-stream unit Reynolds number. In figure 5(a), $\bar{p}_{t,j} = 1.0$, the separation shown is typical of transitional free-interaction separation; that is, the separation point is located in a region of constant geometry (near the intersection of the separation shock wave and the boundary layer), the separation angle is small (the angle between the separation streamline and the body), and transition occurs within the separation region. The Reynolds number based on free-stream Reynolds number per unit length and the distance from the nose to the separation point was 0.5×10^6 . In figure 9(a) for $\bar{p}_{t,j} = 1.0$, 16° cone forebody, and a long centerbody, a flow field is shown at $M_\infty = 3.0$ in which the Reynolds number at separation was 2.3×10^6 , and the separation was of the turbulent free-interaction type; that is, the separation point was located in a region of constant geometry, the separation angle was large, and transition occurred near or before separation. In the case shown, transition may not have occurred before separation but did occur before the shear layer was established. No laminar free-interaction separation was observed in this investigation; the separation point always reached the forebody at the lower Reynolds numbers, even for a low jet pressure as in figure 5(c) ($\bar{p}_{t,j} = 0.1$).

The surface-pressure data corresponding to the example of transitional and turbulent free-interaction separation did not disagree with the conclusions drawn from the photographs. In figure 6(a) (corresponding to fig. 5(a), $\bar{p}_{t,j} = 1.0$), the pressures at orifices 1 and 2 were near free stream and indicated that the separation angle was small, and the surface pressure increased where transition occurred in the shear layer, as expected for transitional free-interaction separation. (See ref. 5.) In figure 10(a), the separation point on the long centerbody occurred very near orifice 3. (See fig. 9(a), $\bar{p}_{t,j} = 1.0$; 16° cone forebody; long centerbody.) It is therefore likely that the surface pressure ratio remains near 1.0 to that point and then jumps to the higher level shown

by orifices 4 and 5 since such a pressure distribution would be expected for turbulent free-interaction separation. (See ref. 5.)

Effect of Jet Pressure

The effects on the flow field of varying the jet pressure are presented in figures 5(a), 5(b), and 5(c), for $M_\infty = 3.0$, 4.5, and 6.0, respectively, for the 30° cone forebody with the short centerbody and all four nozzles firing at $M_j = 3.68$. The corresponding surface pressure data are presented in figure 6 in the form of p/p_∞ plotted as a function of the distance from the base of the model in diameters, x/d .

At $M_\infty = 3.0$ (fig. 5(a)), the separation point was aft of the cone-cylinder juncture for all jet pressures. The separation was of the transitional free-interaction type for $\bar{p}_{t,j} = 0.2$, 1.0, 1.2, and perhaps 0.6. At $\bar{p}_{t,j} = 1.2$, the secondary flow appears to extend forward of and above the confluence of the shear layers, and the extent of separation does not appear to have increased from that at the reference jet pressure. (In order for the secondary flow to extend forward of and above the confluence of the shear layers, some of the primary flow must divide, leave the plane of the model center line and nozzle 1, and flow around the secondary flow between the secondary flows of two adjacent nozzles.) At $\bar{p}_{t,j} = 0.2$, the secondary flow appears to remain attached to the point of maximum forward penetration, and, as a result, there is a stronger interaction with the primary flow than for $\bar{p}_{t,j} = 0.6$. This particular flow field is similar to the flow field which occurs when a jet is exhausted forward from the front of a blunt body at a low jet pressure as reported in reference 6.

At $M_\infty = 4.5$ and $M_\infty = 6.0$ (figs. 5(b) and 5(c)), the separation point of the primary shear layer was located at the cone-cylinder juncture for even the lowest test jet pressures and hence is not of the previously discussed free-interaction type. As the jet pressure was increased, the separation angle increased. This increased angle decreased the expansion around the cone-cylinder juncture. The turning of the bow shock wave by the expansion was therefore less at the higher jet pressures, and the bow shock wave therefore appeared to move outward as a result of increased jet pressure. As expected, the surface pressures (figs. 6(b) and 6(c)) increased with increased separation angle and jet pressure.

Effect of Forebody Shape

The effect of forebody shape on the flow field is shown by the schlieren photographs for $M_\infty = 3.0$, $M_\infty = 4.5$, and $M_\infty = 6.0$ in figures 7(a), 7(b), and 7(c), respectively. The corresponding surface pressures p/p_∞ are plotted against x/d in figure 8.

At $M_\infty = 3.0$, the flat forebody photograph is the only photograph in figure 7(a) in which a laminar shear layer is not visible aft of the separation point and in which the separation is typical of the turbulent free-interaction type. The abruptness of the forebody-cylinder juncture may have an important effect on the location of transition and therefore on the separation characteristics at $M_\infty = 3.0$. The increased length of the 15° cone and ogive forebodies, relative to 30° cone forebody, increased the local Reynolds number at a given distance from the base. The effect of increased length offsets the effect of decreased abruptness to some extent in the comparison of the 30° cone and ogive forebody flow fields. At similar lengths, the flat forebody caused more turbulence (visible in the shear layer) than the 30° cone forebody, and the 15° cone forebody caused more turbulence than the ogive forebody. In comparing the 15° and 30° cone forebody flow fields, the conclusion reached seems to be that the length change is more important at the conditions shown than the juncture change, since transition is both more forward and closer to the separation point for the 15° cone.

The flat forebody flow field has a larger secondary flow at $M_\infty = 6.0$ (fig. 7(c)) than at $M_\infty = 4.5$ (fig. 7(b)), which is expected because p_j/p_∞ is greater at $M_\infty = 6.0$. For the 30° cone, 15° cone, and ogive forebodies, however, the extent of the secondary flow is nearly equal for both free-stream Mach numbers. This result can be understood by realizing that for the flat forebody, the bow shock wave is located far enough from the body to assure that the secondary flow does not affect it at the p_j/p_∞ of $M_\infty = 4.5$, and the secondary flow can expand as p_j/p_∞ is increased. This condition is not true for the pointed forebodies. Because the bow shock wave is attached and therefore located more closely to the body, the secondary flow is more limited in the extent to which it can expand with p_j/p_∞ before affecting the bow shock wave. Once the secondary flow begins to affect the bow-shock-wave location, larger changes in p_j/p_∞ are required for given increases in the extent of the secondary flow. At $M_\infty = 6.0$, the included angle of the bow shock wave is less than that at $M_\infty = 4.5$, and the secondary flow therefore affects the bow shock wave when the extent of the secondary flow is less. The bow shock wave was closest to the body for the 15° cone forebody at $M_\infty = 6.0$ (fig. 7(c)). The secondary flow was so restricted from radial expansion that it pushed farther forward than for any other forebody. This condition caused the expansion at the cone-cylinder juncture to be eliminated and the separation point to move forward on the conical section of the forebody.

The pressures at orifices 1 and 2 for $M_\infty = 3.0$ (fig. 8(a)) were highest for the 15° cone forebody. The extent of flow separation was also maximum for this forebody (schlieren photographs in fig. 7(a)). Likewise, the 30° cone forebody data show the second highest pressure at orifices 1 and 2 and the second largest separated region. The ogive forebody pressure data show a slight increase above jet-off values; this result corresponds to the small separation angle where the shear layer was laminar. The flat forebody pressure data show a negligible increase above jet-off values; this condition corresponds to

the observed turbulent separation aft of orifices 1 and 2. Nearer the jet, however, the forebody had little effect. At $M_\infty = 4.5$ (fig. 8(b)), the pressures reflect the separation angle for the pointed forebodies, and the variation with position along the body is the same for the 15° cone and ogive forebodies as for the 30° cone forebody. The pressure for the flat forebody was the lowest for the forebodies at the forward orifices and raised to the highest at orifice 5. The pressure data for $M_\infty = 6.0$ (fig. 8(c)) show the same trends as that for $M_\infty = 4.5$ but at a higher level of p/p_∞ . This result was expected because p_j/p_∞ was greater at $M_\infty = 6.0$.

Effect of Centerbody Length

The effects of centerbody length on the flow field and surface pressure distribution are given in figures 9 and 10, respectively. The two effects of centerbody length which affect the flow field visibly are first, the increased local Reynolds number at a given distance from the nozzles with the long centerbody, and second, the increased displacement of the bow shock wave from the nozzles with the long centerbody. The increased Reynolds number at $M_\infty = 3.0$ was sufficient to change the type of separation from transitional to turbulent. (See fig. 9(a).) The lower Reynolds number flow on the short centerbody permitted transitional separation which reached the cone-cylinder juncture, whereas the higher Reynolds number flow on the long centerbody did not separate until well aft of the cone-cylinder juncture. The effect of the location of the bow shock wave can be seen in the flow field photographs at $M_\infty = 4.5$ and $M_\infty = 6.0$. (See figs. 9(b) and 9(c).) At the jet pressure shown, the secondary flow extended radially nearly to the bow shock wave for both centerbody lengths. The size of secondary flow field seems to be more nearly proportional to centerbody length than to centerbody or nozzle diameter. The surface pressure distributions at $M_\infty = 4.5$ and $M_\infty = 6.0$ (figs. 10(b) and 10(c)) show that the pressures were considerably lower on the long centerbody. This fact indicates that although the secondary flow extended nearly to the bow shock wave for both centerbodies, there was less modification of the bow-shock-wave location by the jet flow for the long centerbody.

The diameter of the nozzle relative to the length of the centerbody had an important effect on the surface pressures in much the same way that jet pressure did. If the size of the model is normalized by the centerbody length, the nozzles were smaller on the long centerbody configuration and had a smaller effect on the pressures and bow-shock-wave location, but the size of the secondary flow was decreased little.

Effect of Number of Nozzles

Figure 11 shows the effect of the number of nozzles firing on the flow field for the reference jet pressure. The 30° cone forebody, short centerbody, and $M_j = 3.68$ nozzles

were used, and $M_\infty = 3.0$, $M_\infty = 4.5$, and $M_\infty = 6.0$ data are shown in figures 11(a), 11(b), and 11(c), respectively. The corresponding pressure data are shown in figure 12.

At all free-stream Mach numbers, the nozzle 1 firing photographs (fig. 11) indicate that the secondary flow did not separate as sharply from the body (if at all) as with all four nozzles firing. Rather, the secondary flow penetrated farther forward and wrapped around the body to the extent that the primary flow separated from the lower surface of the body as far forward as the cone-cylinder juncture.

The surface pressure distributions (fig. 12) show that the pressure is much higher in the separated region for all four nozzles firing than in the same location with nozzle 1 firing alone. This result would be expected with the decreased separation angle of the secondary flow observed in the schlieren photographs.

Effect of Nozzle Characteristics

Figures 13 to 17 show the effect of varying jet Mach number on the flow field and surface pressure distribution. All the data show that a lower M_j nozzle had a greater effect on the flow field than a higher M_j nozzle at a given $\bar{p}_{t,j}$. This result might be expected because the reference for jet pressure was a total pressure measured in the plenum chamber, and the static pressure at the jet exit (and p_j/p_∞) decreased as M_j increased. Also, the nozzle throat area decreases as M_j increases for fixed jet-exit area, as was the case in this investigation; therefore, the nozzle mass flux decreased with increased M_j . The jet-exit velocity, however, increases with M_j and would be expected to increase the effect of the nozzle on the flow field. The momentum flux and energy flux at the nozzle exit decrease as M_j increases, but only because of the decrease in mass flux. The conclusion can therefore be drawn that for the situation of this investigation, the effects of jet static pressure and mass flux dominated the effect of jet velocity in determining the degree to which the secondary flow interfered with the primary flow.

Correlation of Impingement Pressure Data

In reference 3, the pressure at the orifice just forward of the nozzle (orifice 6 for this test) was found to vary linearly with jet static pressure at a fixed M_j . The pressure coefficient of this orifice based on jet exit conditions was found to be independent of p_j/p_∞ and free-stream Mach number. By modifying this pressure coefficient by a function of jet Mach number and plotting the modified pressure coefficient against p_j/p_∞ , all the data fell close to a single straight line. The slope of the straight line provided an empirical constant which was used to write an equation relating the pressure at orifice 6 to the jet-exit static pressure.

Figure 18 shows the extent to which $C_{p,6}$ was independent of $p_{t,j}$ and of free-stream Mach number, and therefore of p_j/p_∞ , which varied with $p_{t,j}$ and with M_∞ . The data are for the 30° cone forebody and the short centerbody with nozzle 1 firing. In all cases, $C_{p,6}$ was independent of $p_{t,j}$ and M_∞ at the highest jet pressures (when p_j/p_∞ is calculated for these points based on nominal M_j and p_∞ , it is found to be greater than 50) and had a distinct mean value for each jet Mach number. The flow in the impingement region is therefore similar to static test results for underexpanded free jets impinging upon an adjacent surface as reported in reference 7. All points with $C_{p,6}$ less negative than the mean represent conditions with p_j/p_∞ less than 10, and the change is probably due to the higher relative p_∞ . All points with $C_{p,6}$ more negative than the mean represent conditions with p_j/p_∞ between 10 and 50.

Figures 19 and 20 show a comparison of the present results with those of reference 3. Because p_6 does not measure the maximum surface pressure and is difficult to measure because it is located in a region of a steep pressure gradient, further effort to correlate p_6 data has not been attempted.

SUMMARY OF RESULTS

Some of the effects of supersonic conical nozzles exhausting into an oncoming stream near a large cylindrical body have been investigated for free-stream Mach numbers of 3.0, 4.5, and 6.0. The results may be summarized as follows:

1. The location of the bow shock wave at jet-off conditions was important in determining the extent of the secondary flow.
2. When the separation occurred at the forebody-cylinder juncture, the level of the surface pressure was closely related to the separation angle.
3. When the separation occurred on the cylindrical section of the model, it was free interaction and both transitional and turbulent types appeared to exist, depending on local Reynolds number.
4. Jet stagnation pressure, static pressure, and jet mass flux appeared to be the dominant nozzle parameters in determining the extent to which the secondary flow affected the flow field.

5. The surface pressure just forward of the nozzle did not depend on free-stream conditions and therefore was similar to static test results for underexpanded free jets impinging upon an adjacent surface, except for ratios of jet-exit static pressure to free-stream static pressure less than 50.

Langley Research Center,
National Aeronautics and Space Administration,
Hampton, Va., November 18, 1970.

REFERENCES

1. McGhee, Robert J.: Some Effects of Jet Pluming on the Static Stability of Ballistic Bodies at a Mach Number of 6.00. NASA TN D-3698, 1966.
2. Hinson, William F.; and McGhee, Robert J.: Effects of Jet Pluming on the Static Stability of Five Rocket Models at Mach Numbers of 4, 5, and 6 and Static Pressure Ratios Up To 26 000. NASA TN D-4064, 1967.
3. McGhee, Robert J.; and Martin, James A.: Exploratory Investigation of Flow Field Resulting From Forward-Facing Nozzles Exhausting Near a Large Cylindrical Body at Free-Stream Mach Numbers of 3.0 and 6.0. NASA TN D-5030, 1969.
4. Stokes, George M.: Description of a 2-Foot Hypersonic Facility at the Langley Research Center. NASA TN D-939, 1961.
5. Chapman, Dean R.; Kuehn, Donald M.; and Larson, Howard K.: Investigation of Separated Flows in Supersonic and Subsonic Streams With Emphasis on the Effect of Transition. NACA Rep. 1356, 1958.
6. Romeo, David J.; and Sterrett, James R.: Exploratory Investigation of the Effect of a Forward Facing Jet on the Bow Shock of a Blunt Body in a Mach Number 6 Free Stream. NASA TN D-1605, 1963.
7. Vick, Allen R.; and Andrews, Earl H., Jr.: An Experimental Investigation of Highly Underexpanded Free Jets Impinging Upon a Parallel Flat Surface. NASA TN D-2326, 1964.

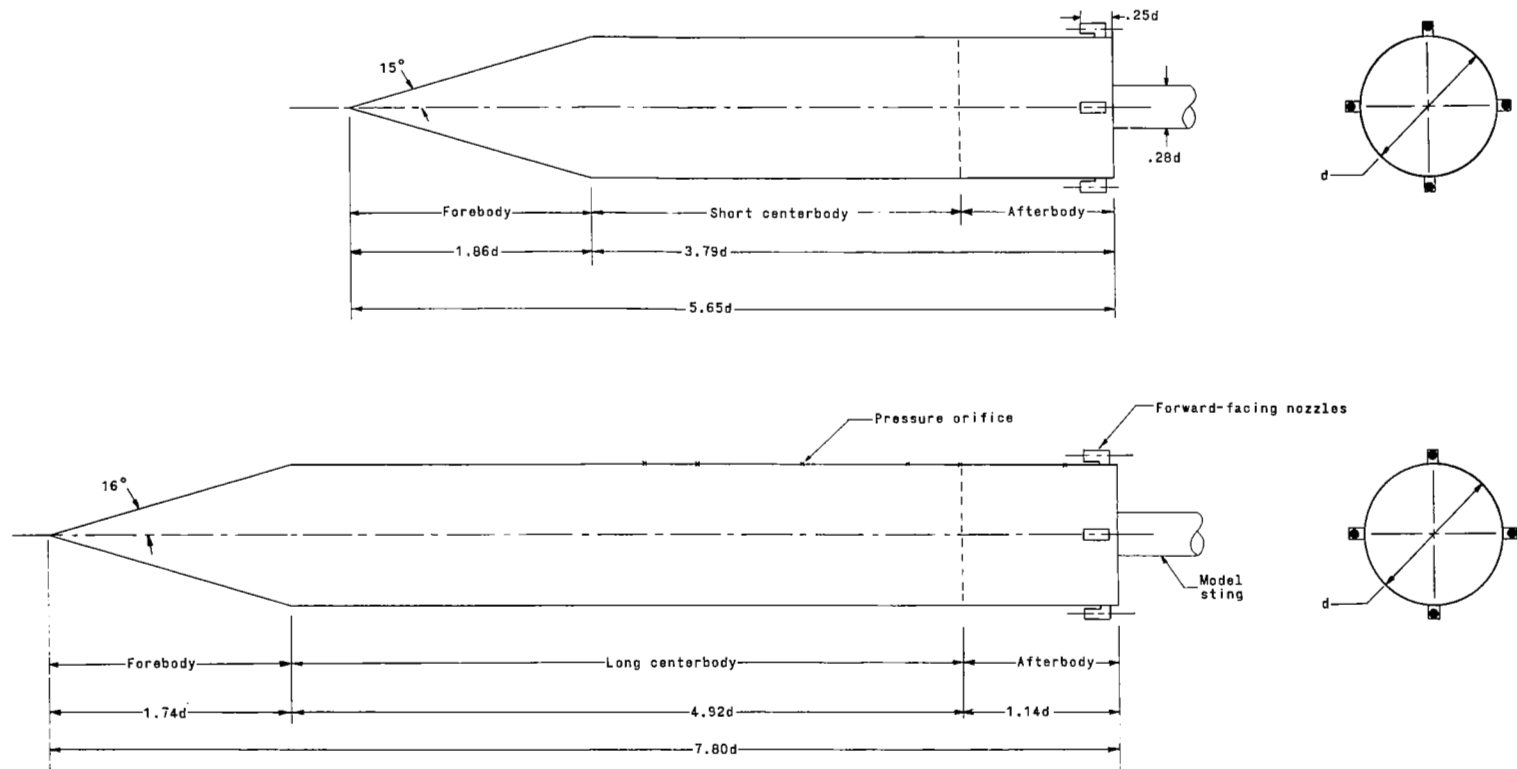


Figure 1.- General model arrangement. $d = 6.71 \text{ cm}$ (2.64 in.)

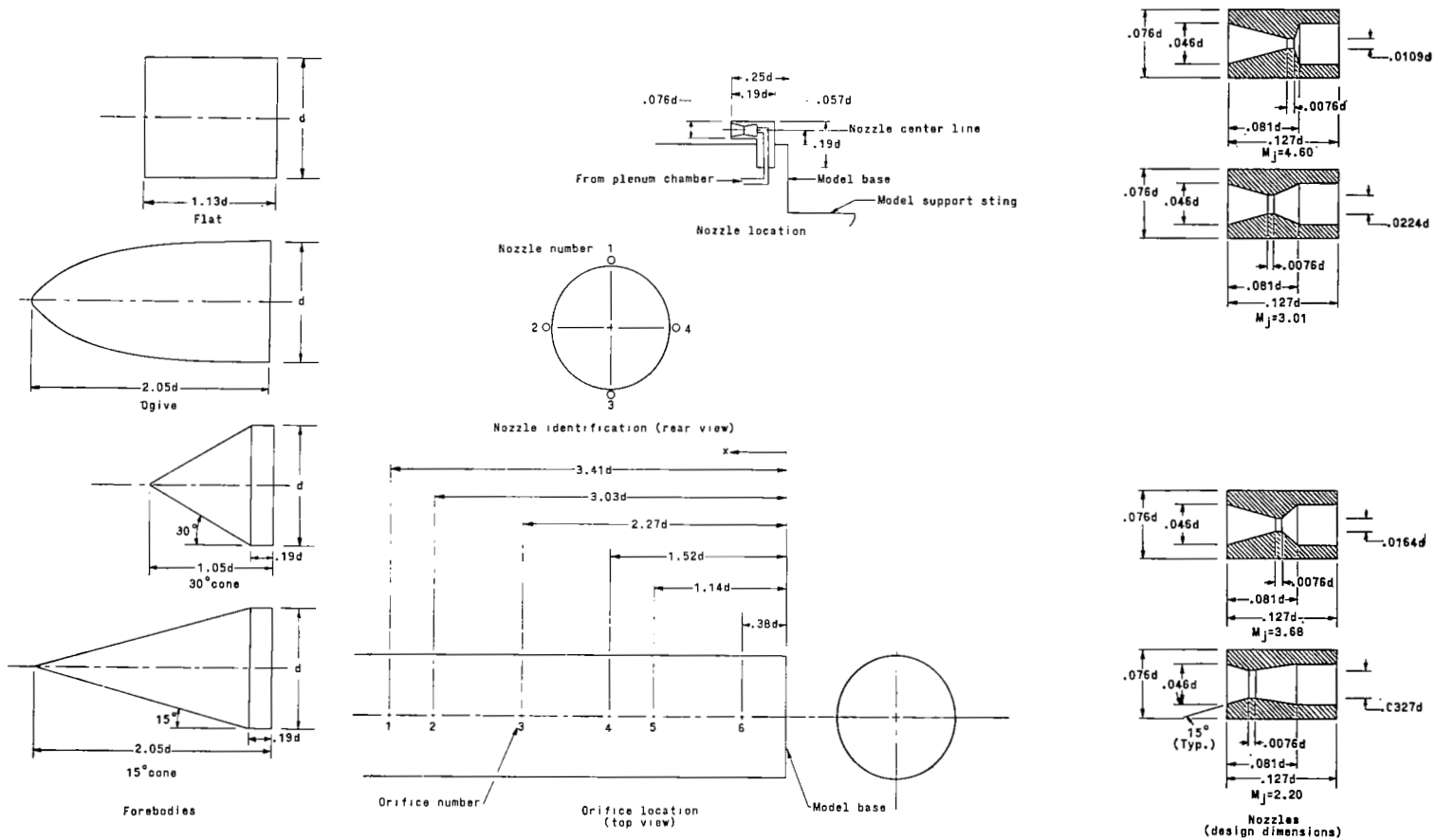


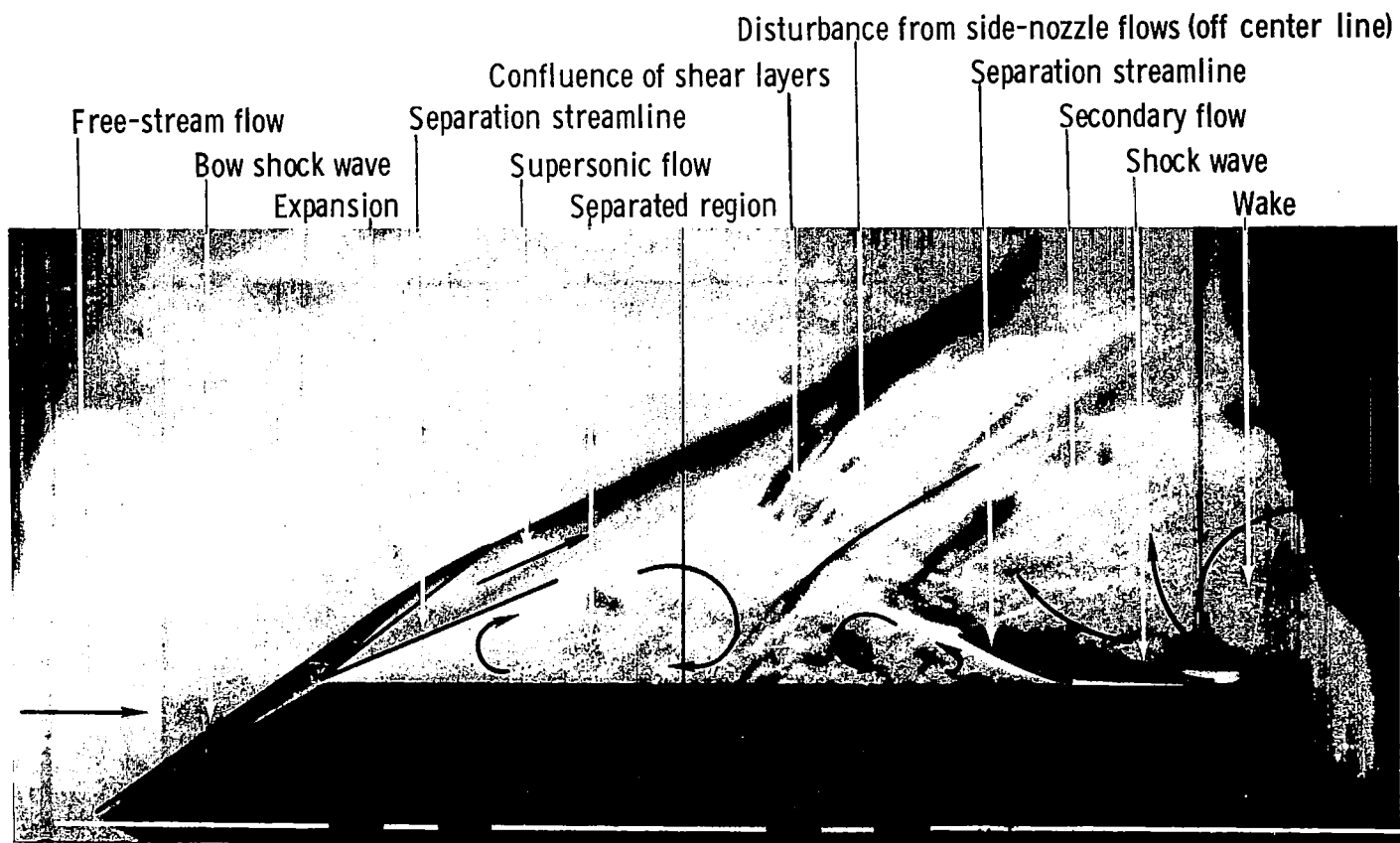
Figure 2.- Model details and orifice locations. $d = 6.71$ cm (2.64 in.).



L-70-8002

(a) Schlieren photograph.

Figure 3.- Flow field for basic test condition at $M_\infty = 6.0$. Reference jet pressure; 30° cone forebody; short centerbody; all four nozzles firing; $M_j = 3.68$.



L-70-8003

(b) Schematic representation.

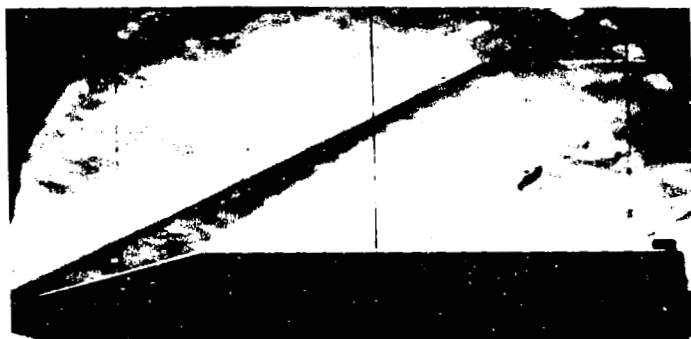
Figure 3.- Concluded.



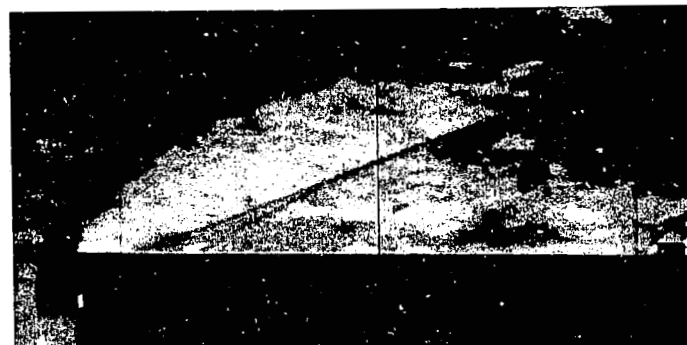
30° cone



Ogive



15° cone

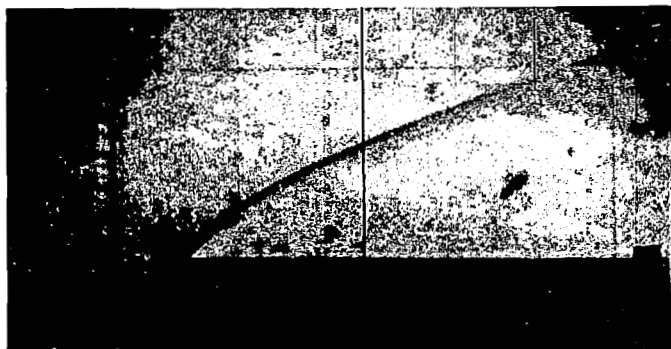


Flat

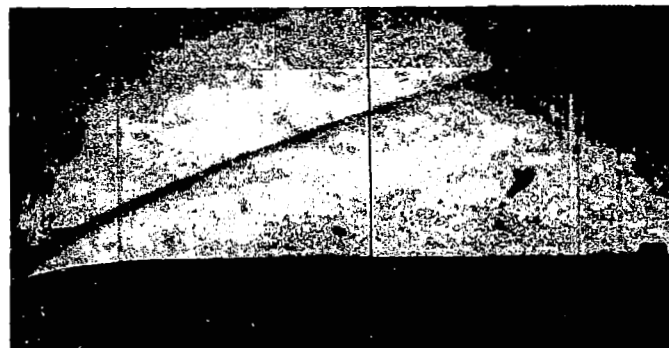
L-70-8004

(a) $M_\infty = 3.0$.

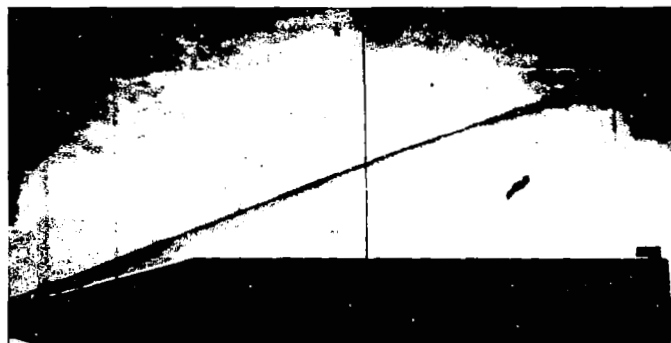
Figure 4.- Effect of forebody shape on the flow field for jet off. Short centerbody.



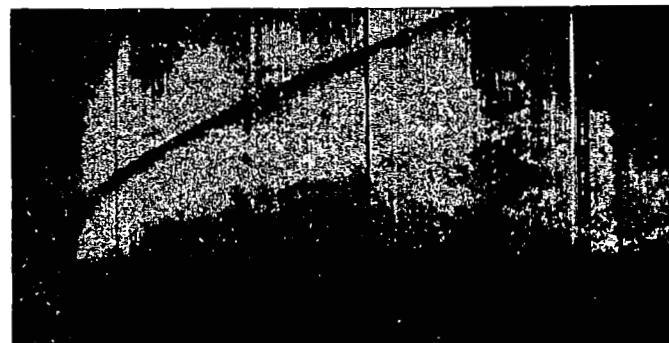
30° cone



Ogive



15° cone

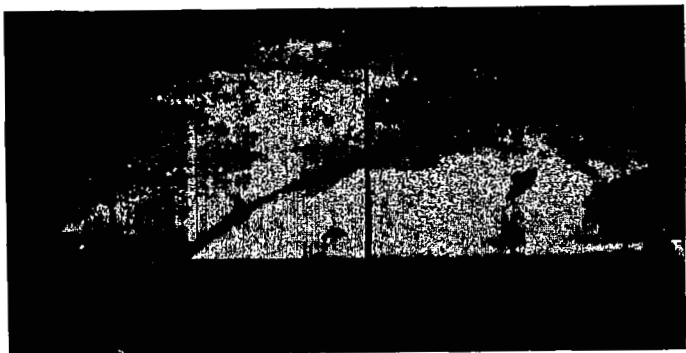


Flat

L-70-8005

(b) $M_\infty = 4.5$.

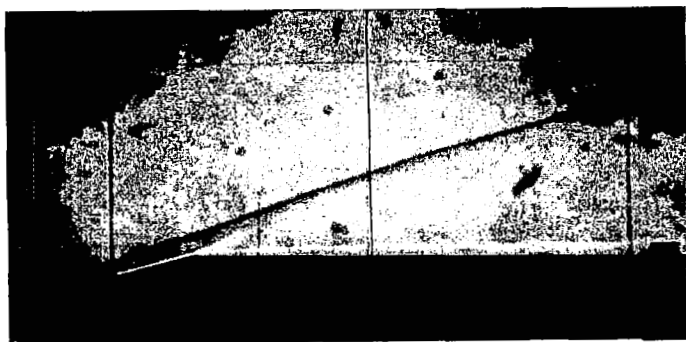
Figure 4.- Continued.



30° cone



Ogive



15° cone



Flat

(c) $M_\infty = 6.0$.

Figure 4.- Concluded.

L-70-8006



$$\bar{p}_{t,j} = 1.2$$



$$\bar{p}_{t,j} = 0.6$$



$$\bar{p}_{t,j} = 1.0$$



$$\bar{p}_{t,j} = 0.2$$

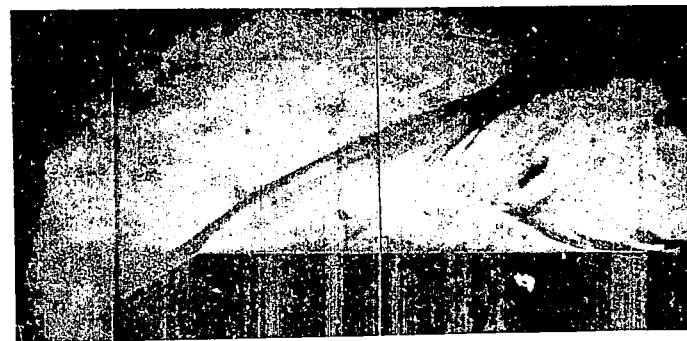
L-70-8007

(a) $M_\infty = 3.0$.

Figure 5.- Effect of jet pressure on the flow field. 30° cone forebody; short centerbody; all four nozzles firing; $M_j = 3.68$.



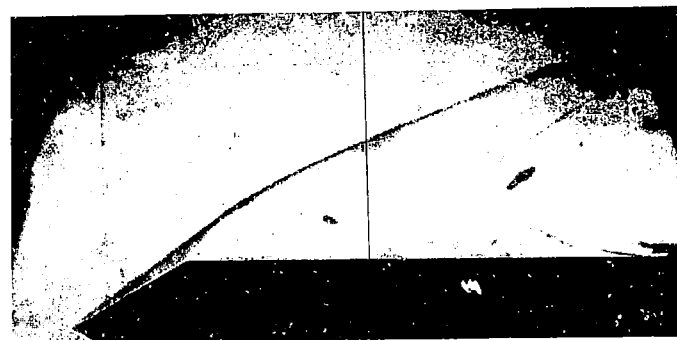
$$\bar{p}_{t,j} = 1.2$$



$$\bar{p}_{t,j} = 0.6$$



$$\bar{p}_{t,j} = 1.0$$



$$\bar{p}_{t,j} = 0.1$$

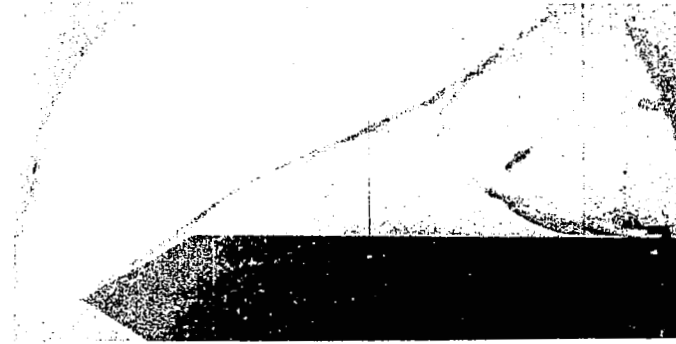
L-70-8008

(b) $M_\infty = 4.5$.

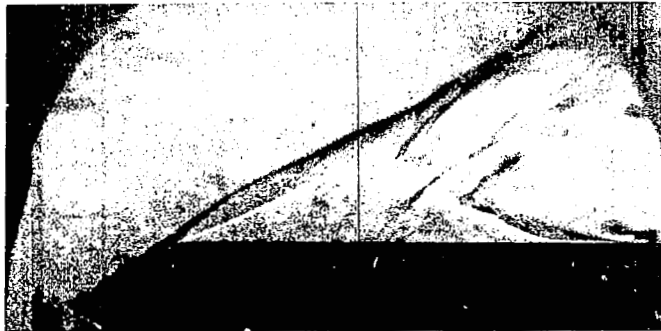
Figure 5.- Continued.



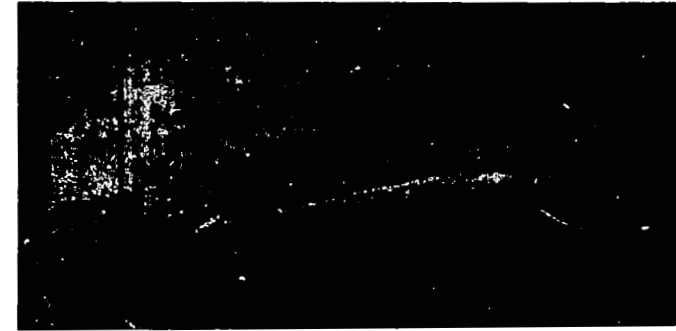
$$\bar{p}_{t,j} = 1.1$$



$$\bar{p}_{t,j} = 0.6$$



$$\bar{p}_{t,j} = 1.0$$

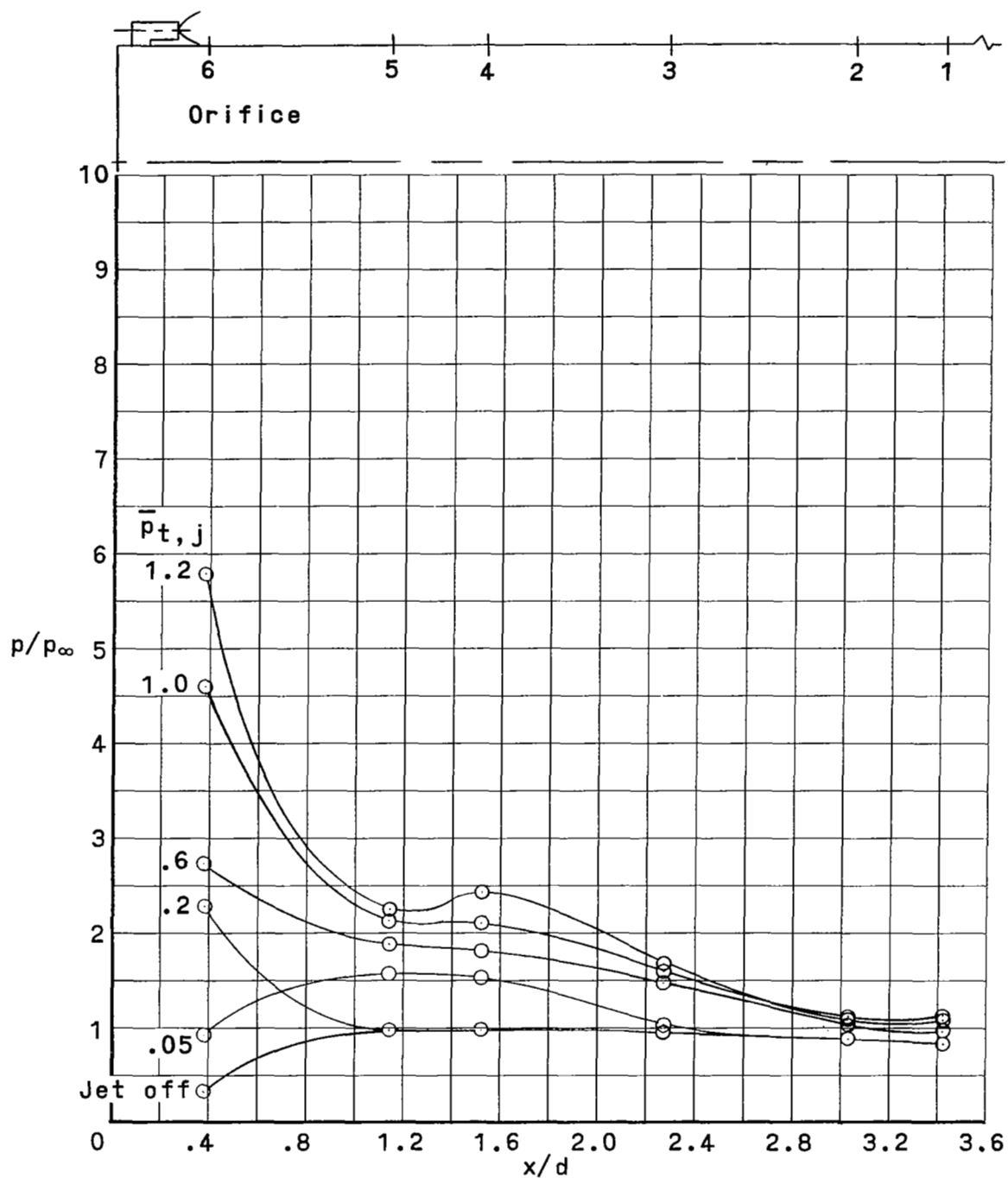


$$\bar{p}_{t,j} = 0.1$$

(c) $M_\infty = 6.0$.

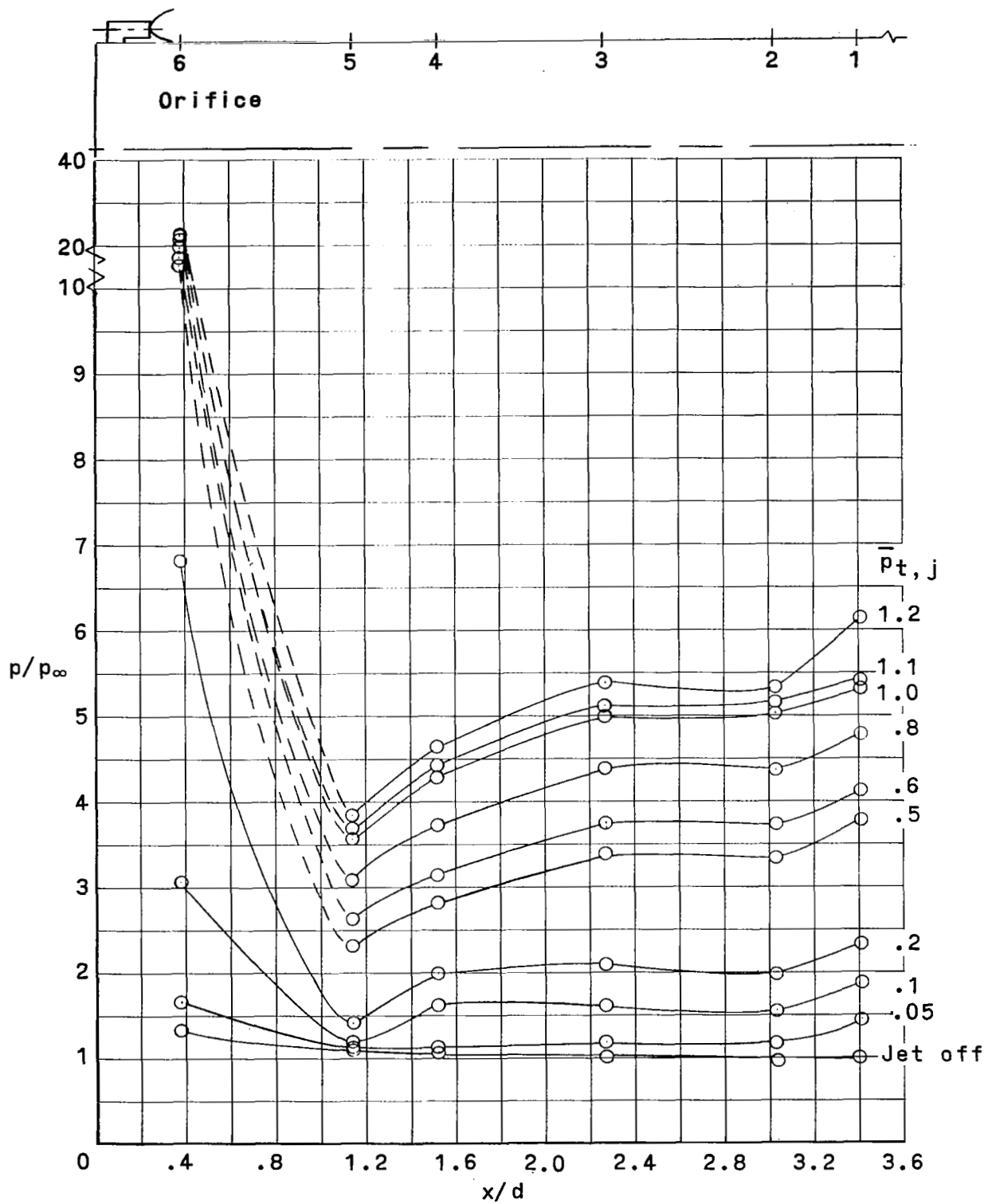
L-70-8009

Figure 5.- Concluded.



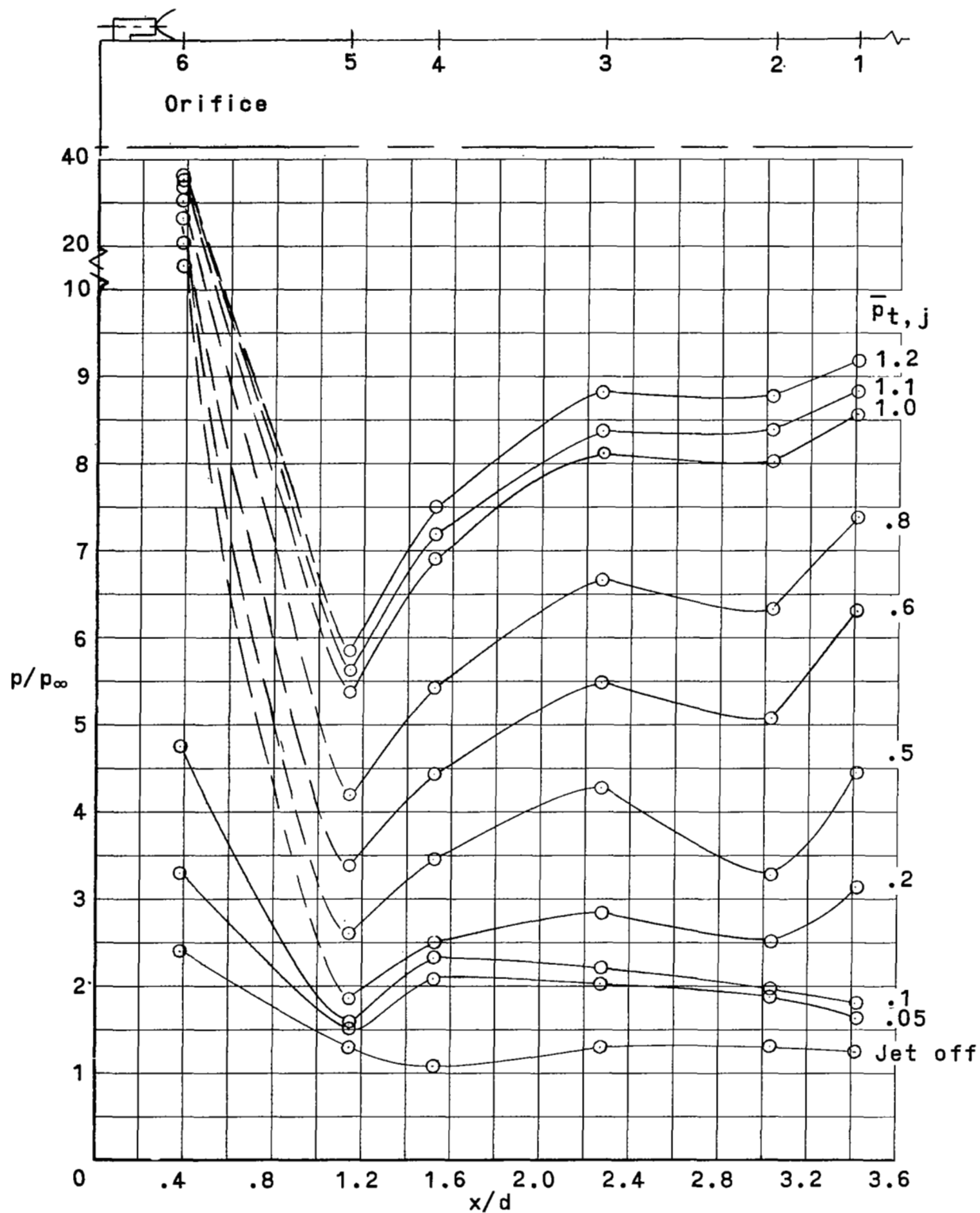
(a) $M_\infty = 3.0$.

Figure 6.- Effect of jet pressure on the surface pressure distribution. 30° cone forebody; short centerbody; all four nozzles firing; $M_j = 3.68$.



(b) $M_\infty = 4.5$.

Figure 6.- Continued.



(c) $M_\infty = 6.0$.

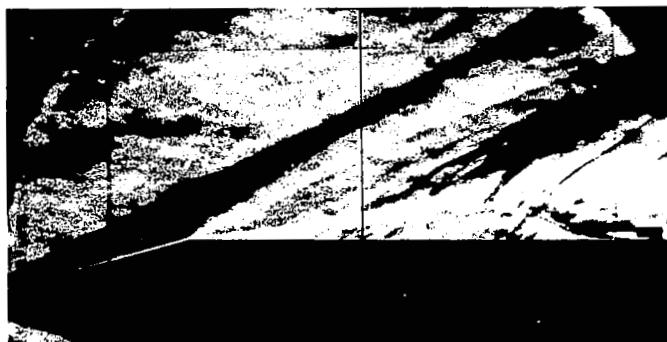
Figure 6.- Concluded.



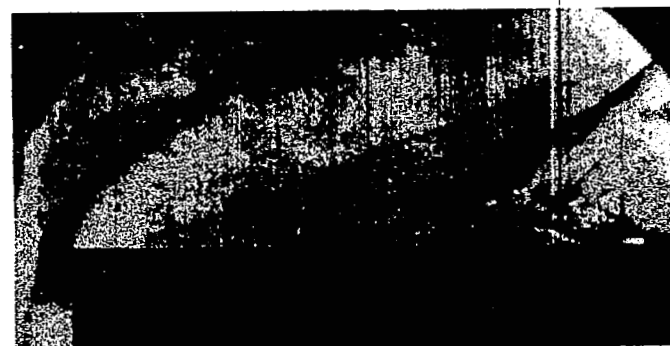
30° cone



Ogive



15° cone



Flat

L-70-8010

(a) $M_\infty = 3.0$.

Figure 7.- Effect of forebody shape on the flow field for reference jet pressure. Short centerbody;
all four nozzles firing; $M_j = 3.68$.



30° cone



Ogive



15° cone



Flat

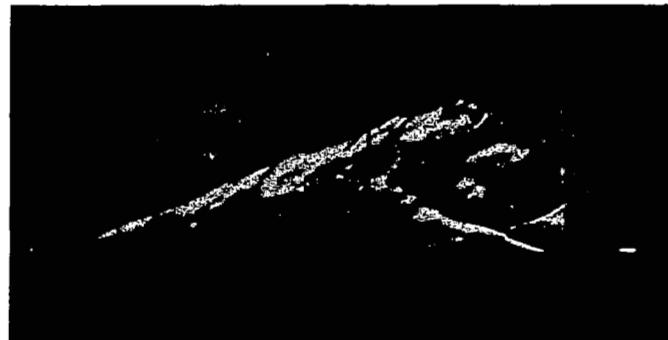
(b) $M_\infty = 4.5$.

Figure 7.- Continued.

L-70-8011



30° cone



Ogive



15° cone

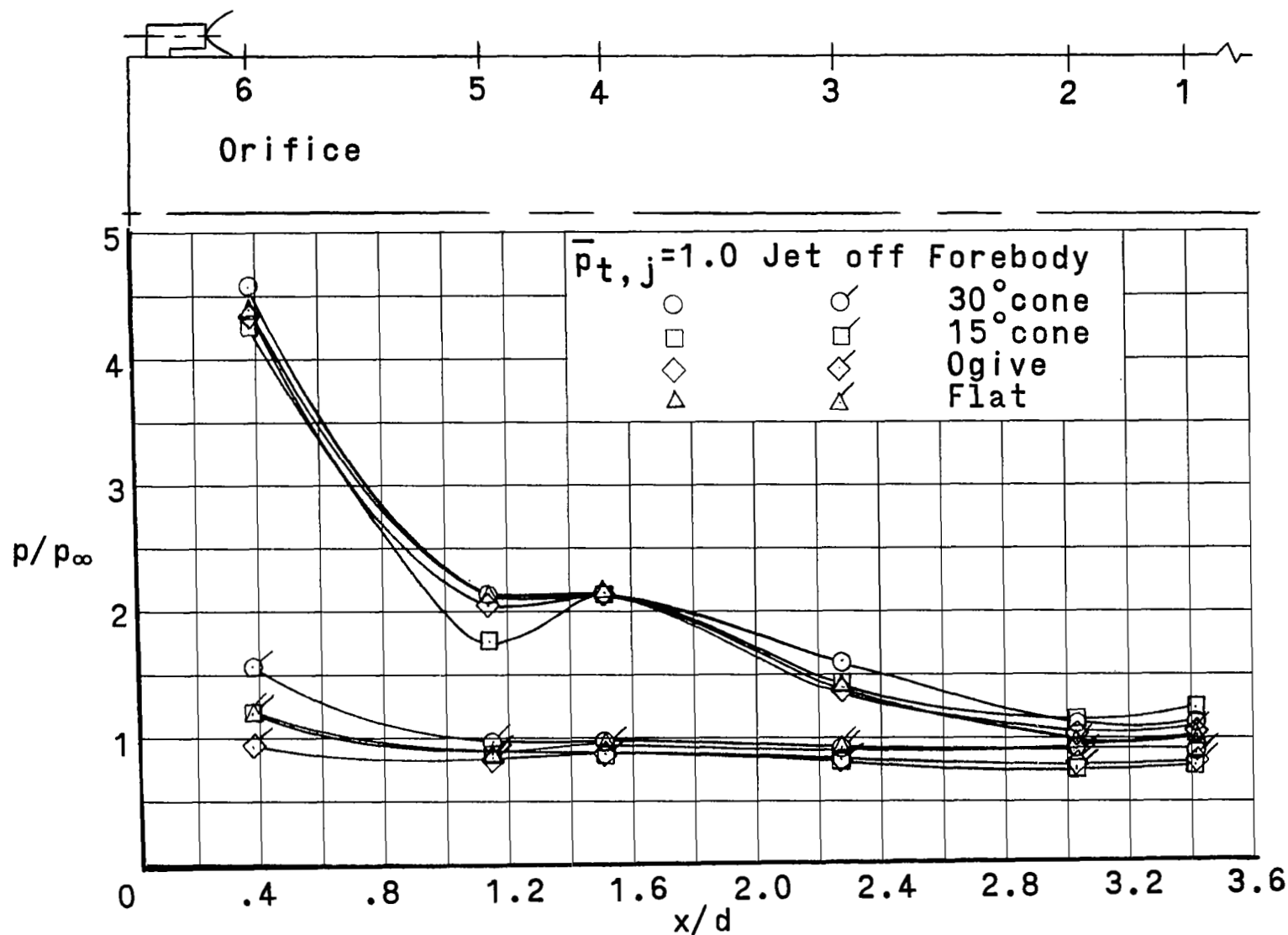


Flat

(c) $M_\infty = 6.0$.

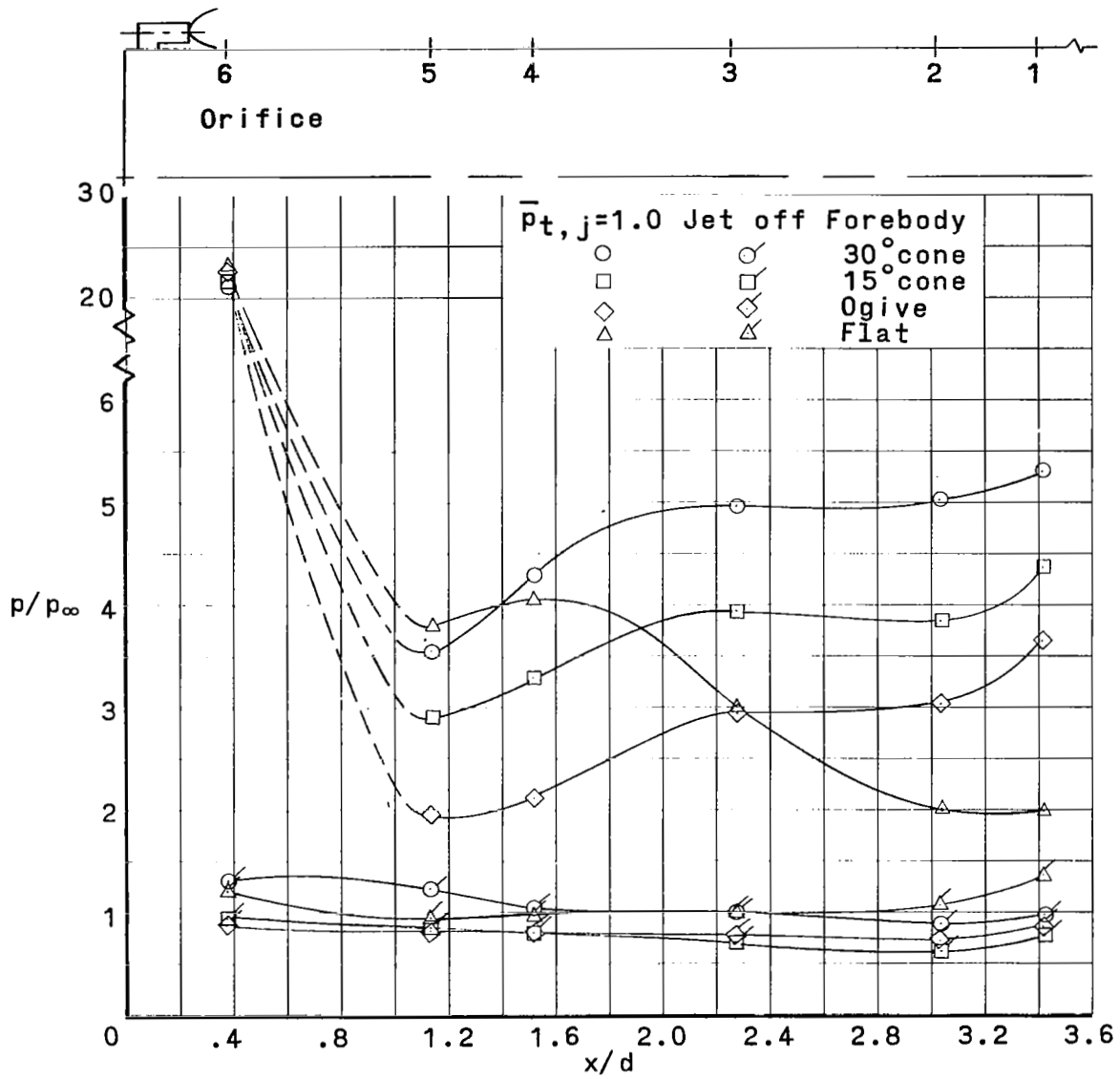
Figure 7.- Concluded.

L-70-8012



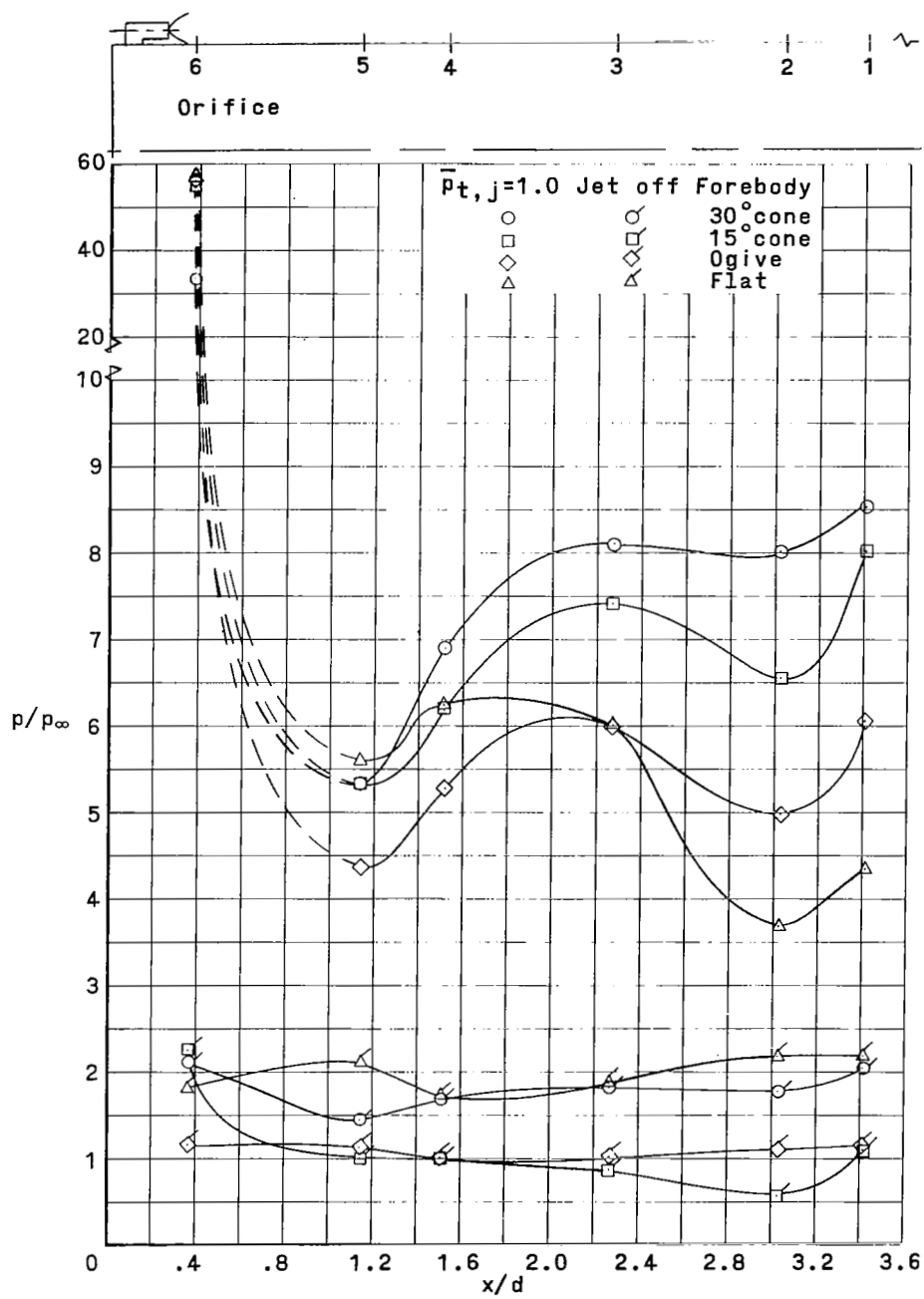
(a) $M_\infty = 3.0$.

Figure 8.- Effect of forebody shape on the surface pressure distribution for reference jet pressure and for jet off.
Short centerbody; all four nozzles firing; $M_j = 3.68$.



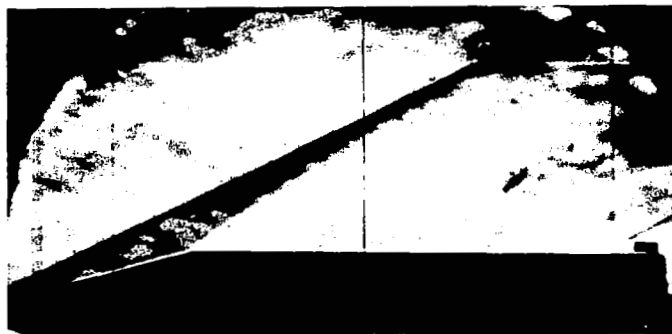
(b) $M_\infty = 4.5$.

Figure 8.- Continued.



(c) $M_\infty = 6.0$.

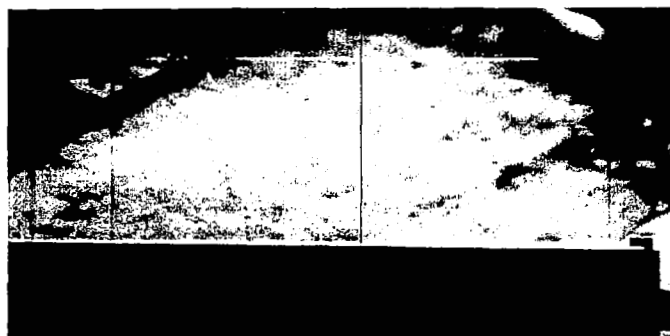
Figure 8.- Concluded.



Jet off; 15° cone forebody; short centerbody



$\bar{p}_{t,j} = 1.0$; 15° cone forebody; short centerbody



Jet off; 16° cone forebody; long centerbody

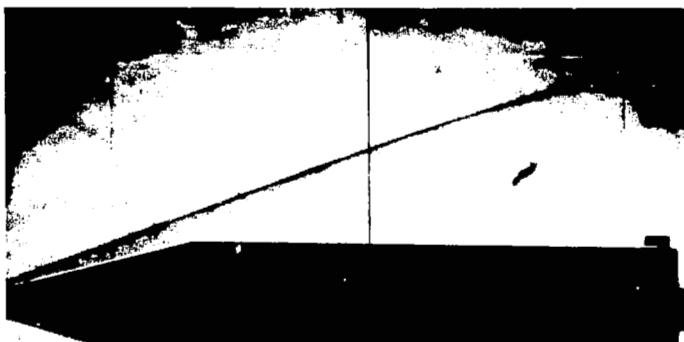


$\bar{p}_{t,j} = 1.0$; 16° cone forebody; long centerbody

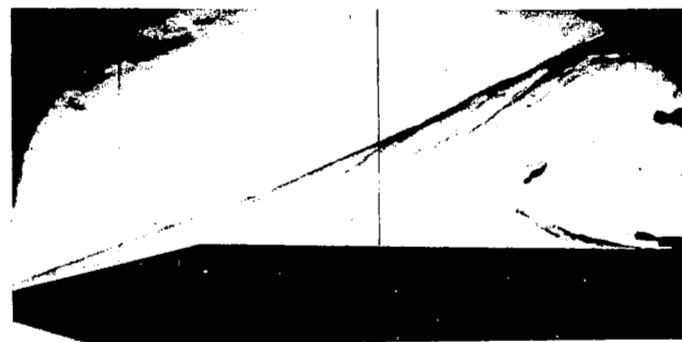
L-70-8013

(a) $M_\infty = 3.0$.

Figure 9.- Effect of centerbody length on the flow field for reference jet pressure and for jet off.
All four nozzles firing; $M_j = 3.68$.



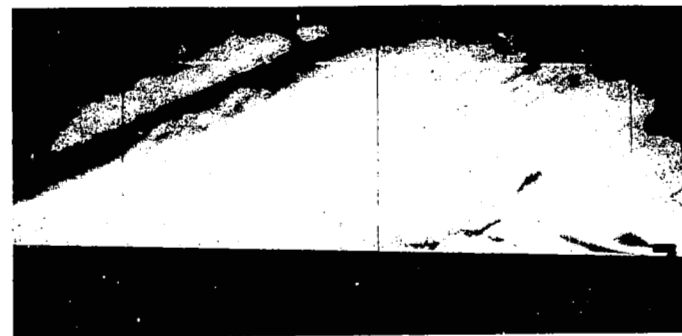
Jet off; 15° cone forebody; short centerbody



$\bar{p}_{t,j} = 1.0$; 15° cone forebody; short centerbody



Jet off; 16° cone forebody; long centerbody



$\bar{p}_{t,j} = 1.0$; 16° cone forebody; long centerbody

L-70-8014

(b) $M_\infty = 4.5$.

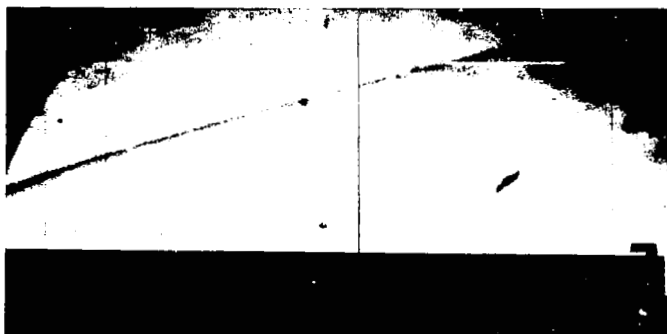
Figure 9.- Continued.



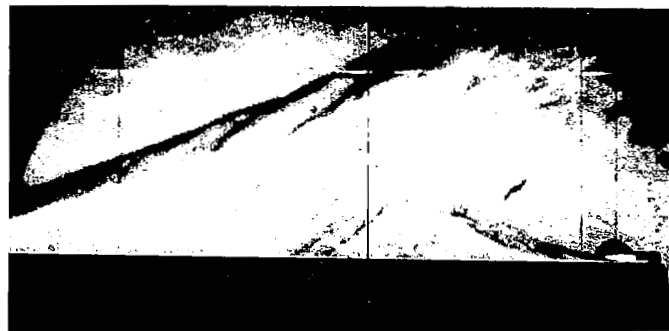
Jet off; 15° cone forebody; short centerbody



$\bar{p}_{t,j} = 1.0$; 15° cone forebody; short centerbody



Jet off; 16° cone forebody; long centerbody

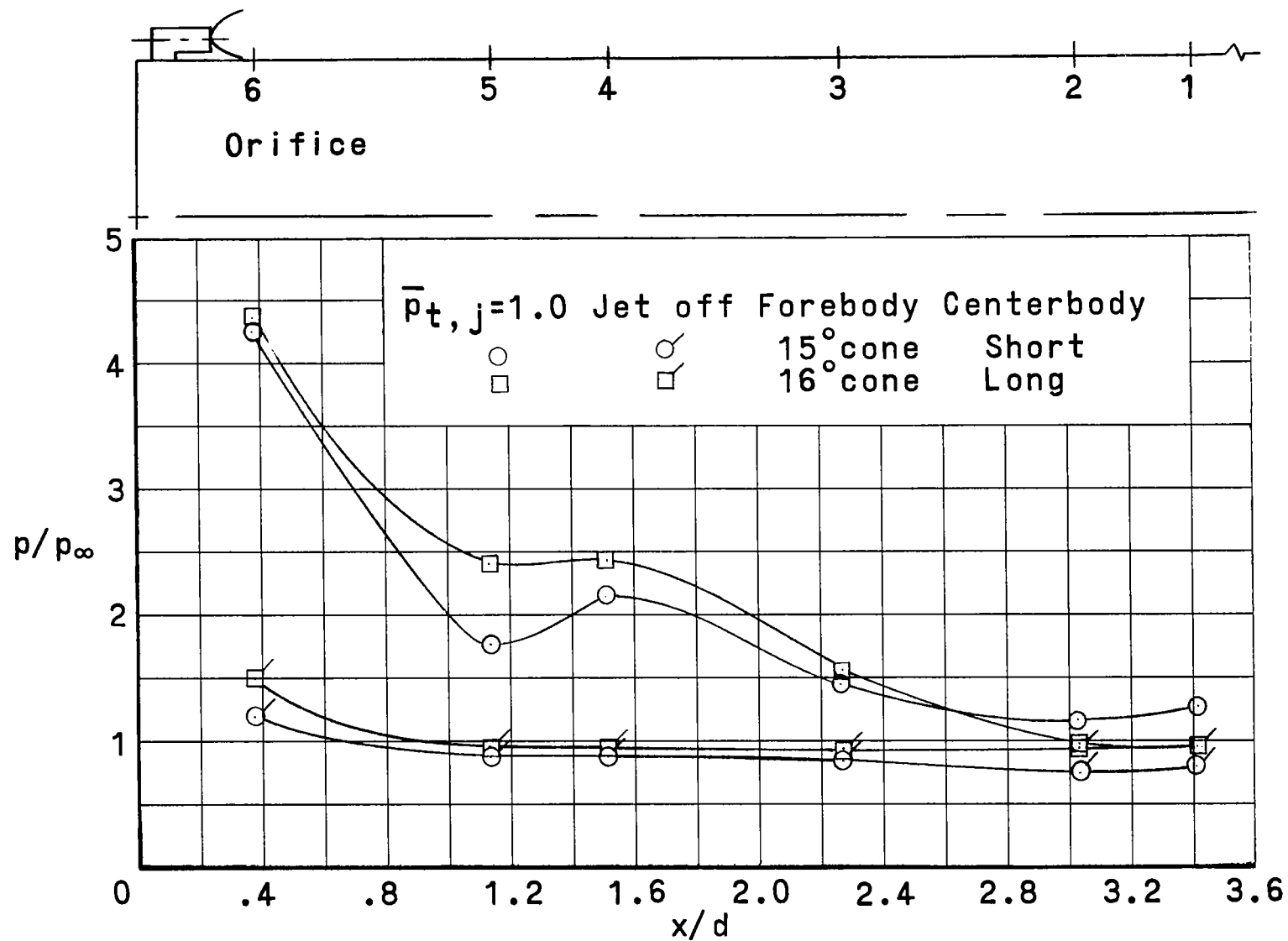


$\bar{p}_{t,j} = 1.0$; 16° cone forebody; long centerbody

L-70-8015

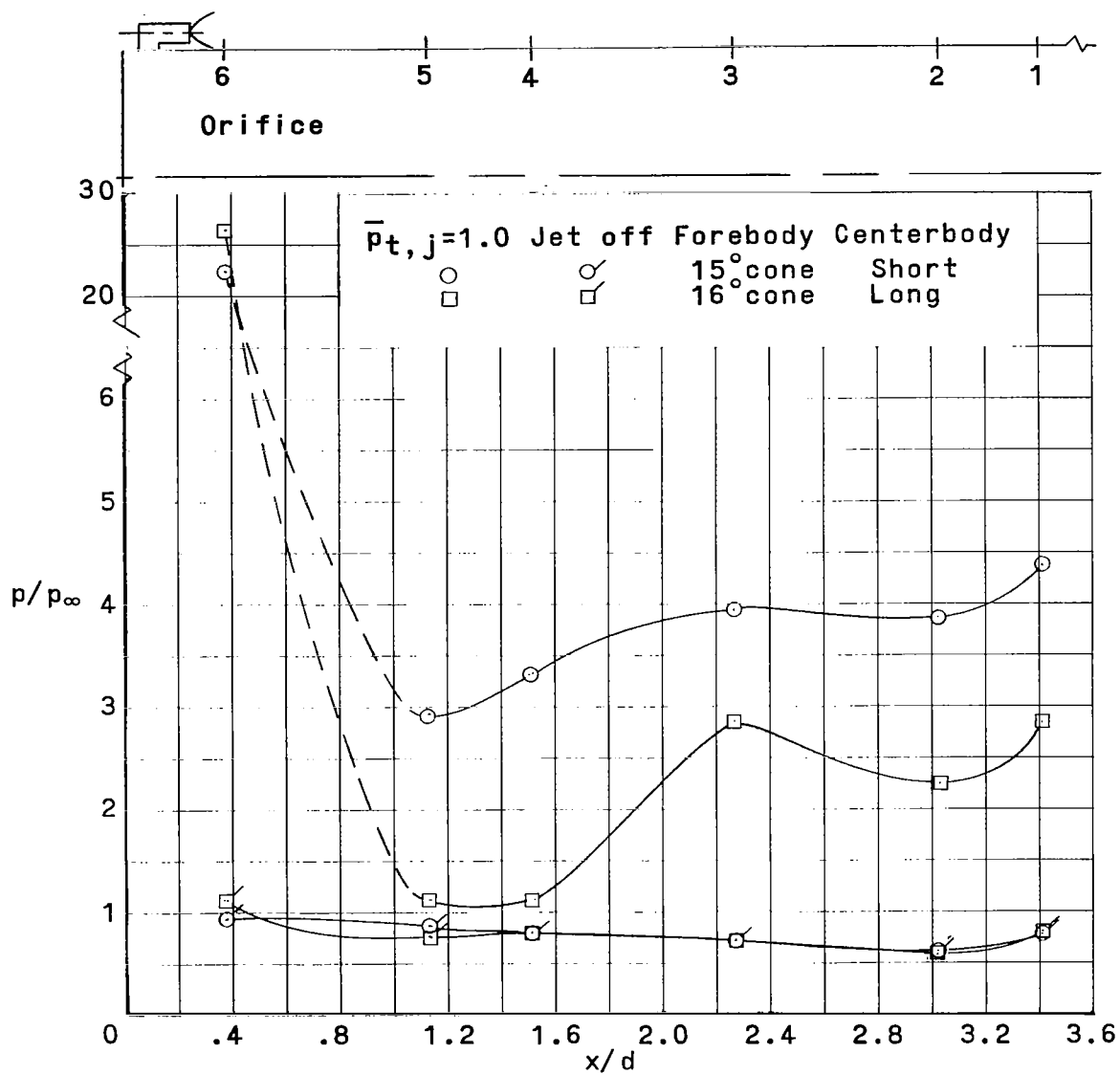
(c) $M_\infty = 6.0$.

Figure 9.- Concluded.



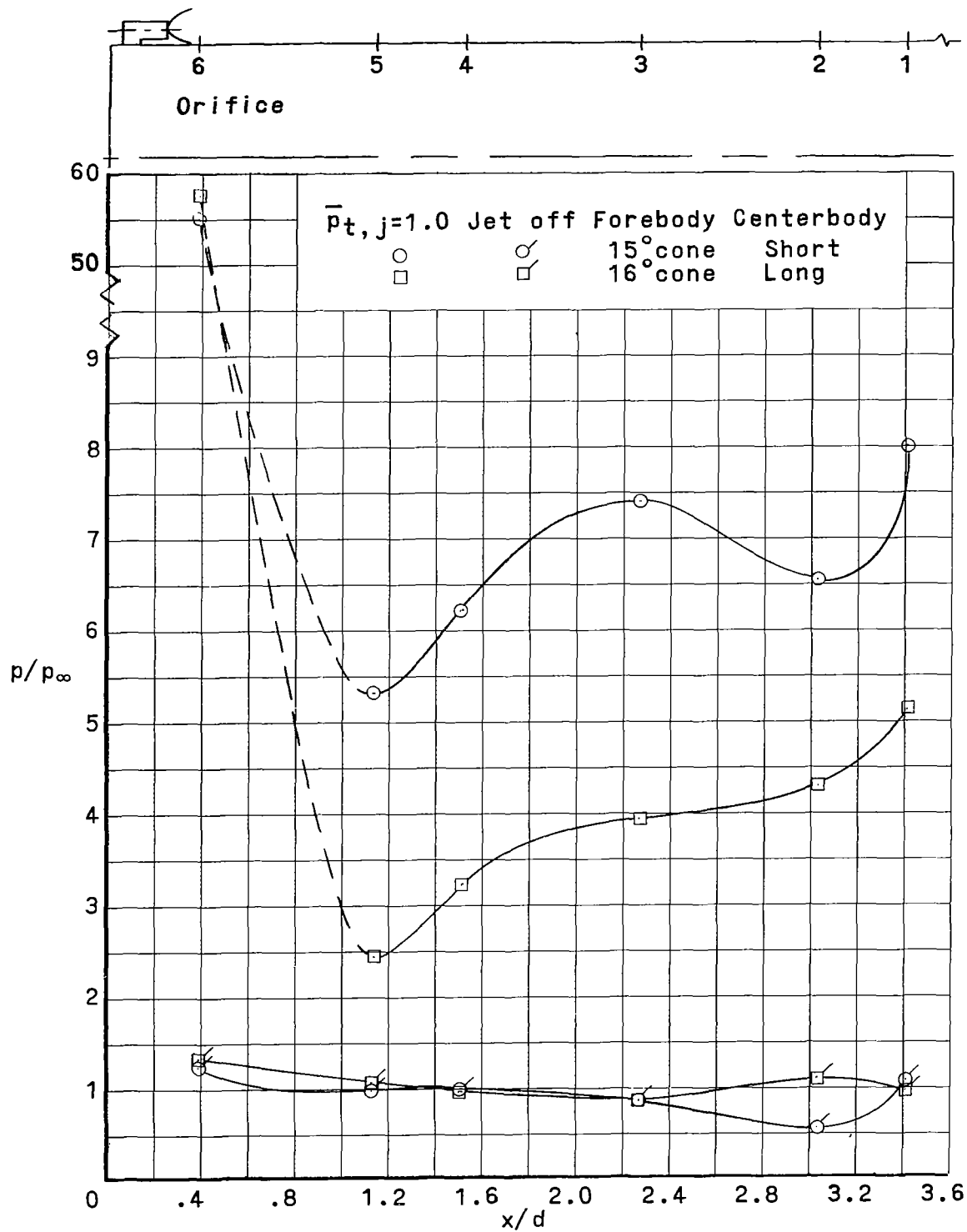
(a) $M_\infty = 3.0$.

Figure 10.- Effect of centerbody length on the surface pressure distribution for reference jet pressure and for jet off. All four nozzles firing; $M_j = 3.68$.



(b) $M_\infty = 4.5$.

Figure 10.- Continued.



(c) $M_\infty = 6.0$.

Figure 10.- Concluded.



Nozzles 1, 2, 3, 4 firing



Nozzle 1 firing

L-70-8016

(a) $M_\infty = 3.0$.

Figure 11.- Effect of number of nozzles firing on the flow field for reference jet pressure. 30° cone forebody; short centerbody; $M_j = 3.68$.



Nozzles 1, 2, 3, 4 firing



Nozzle 1 firing

L-70-8017

(b) $M_{\infty} = 4.5$.

Figure 11.- Continued.



Nozzles 1, 2, 3, 4 firing

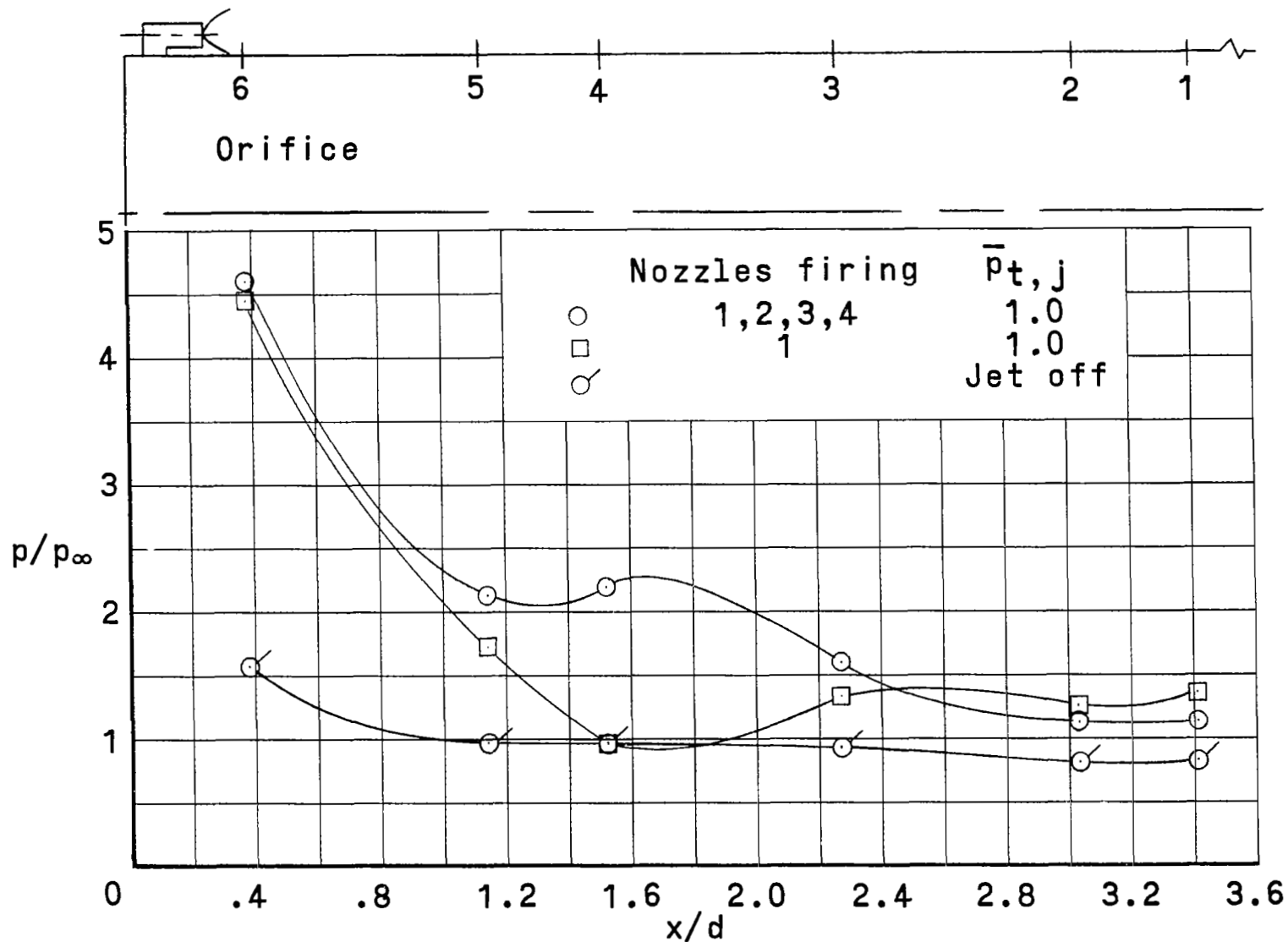


Nozzle 1 firing

(c) $M_{\infty} = 6.0$.

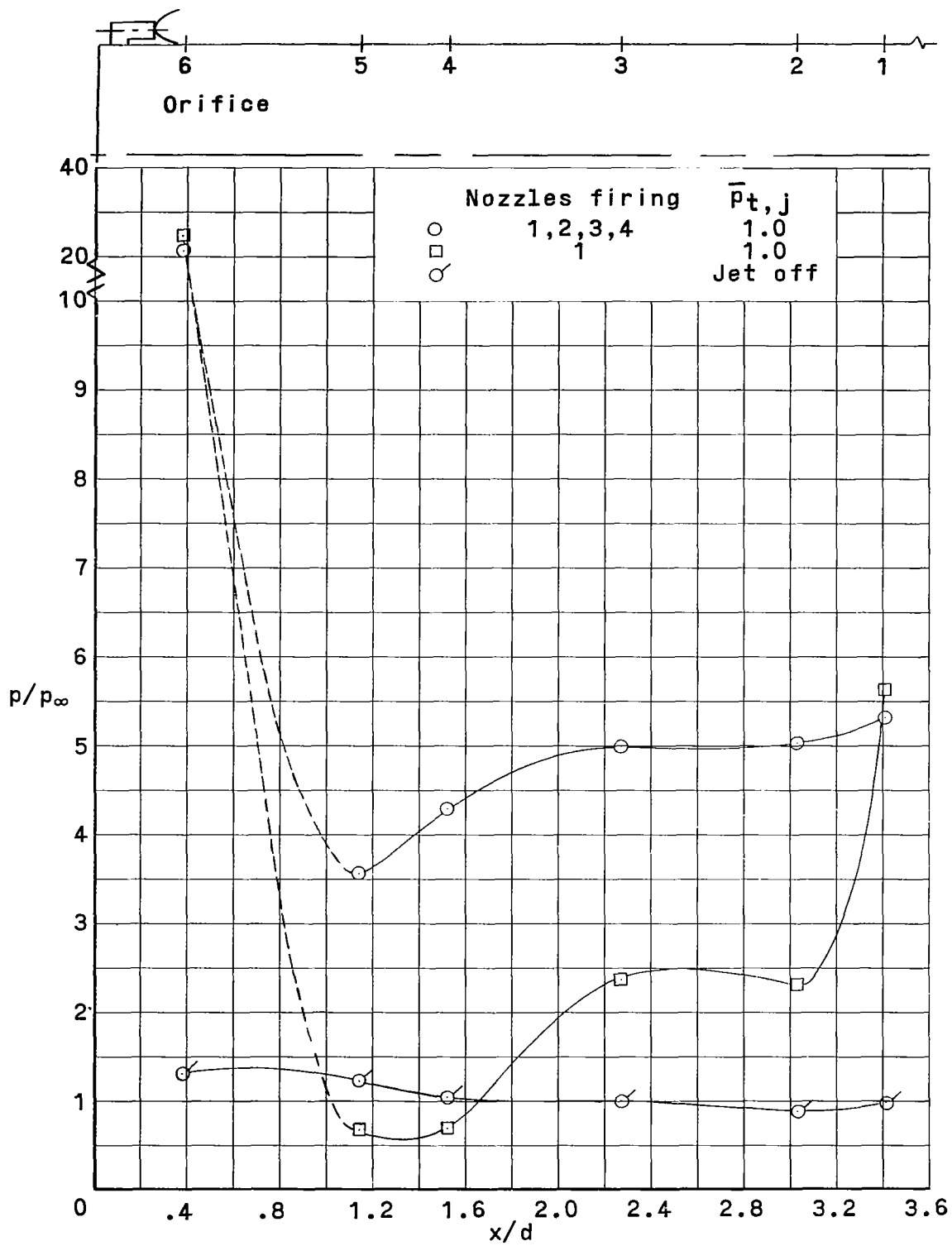
L-70-8018

Figure 11.- Concluded.



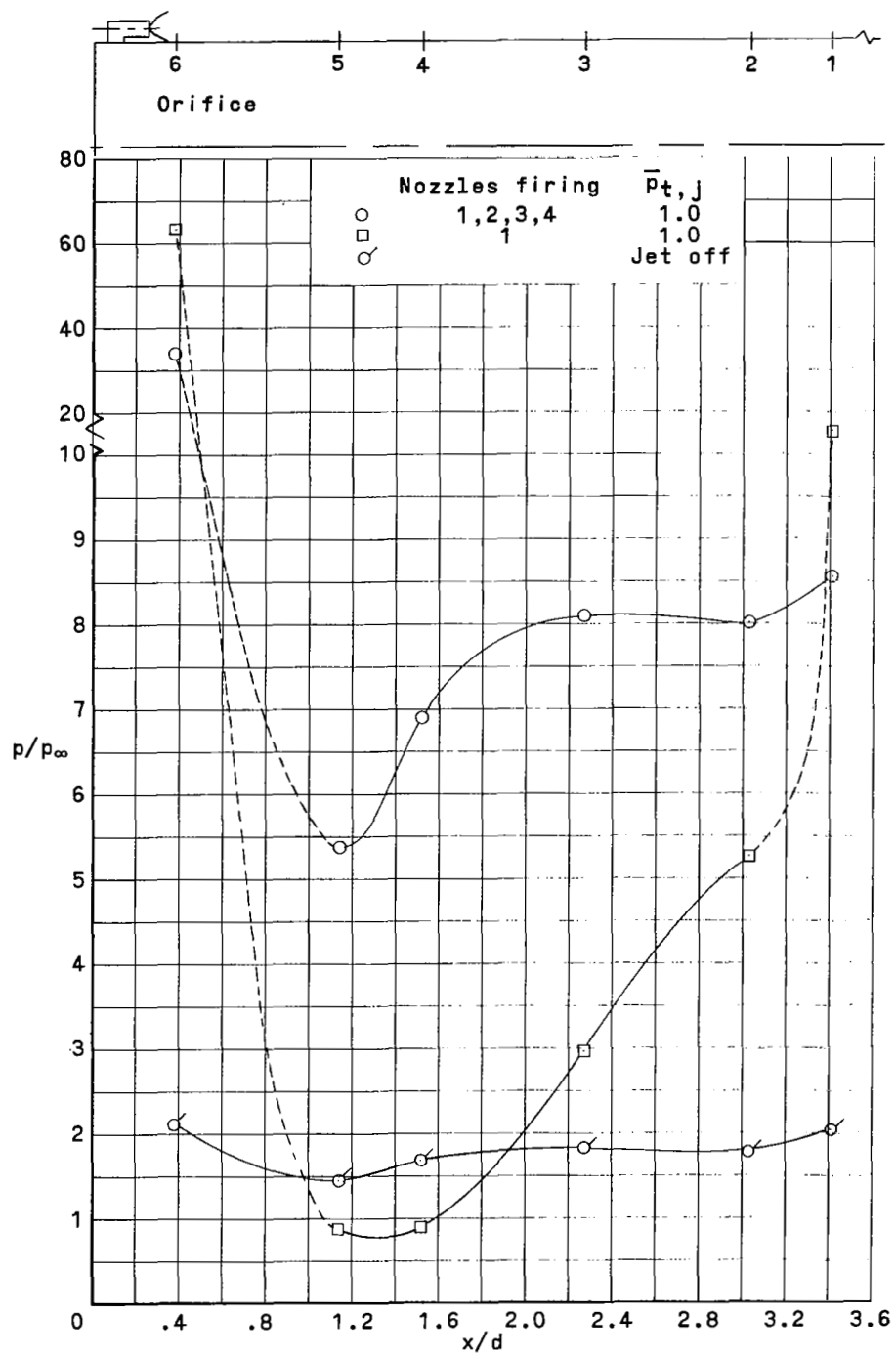
(a) $M_\infty = 3.0$.

Figure 12.- Effect of number of nozzles firing on the surface pressure distribution for reference jet pressure. Jet-off data included; 30° cone forebody; short centerbody; $M_j = 3.68$.



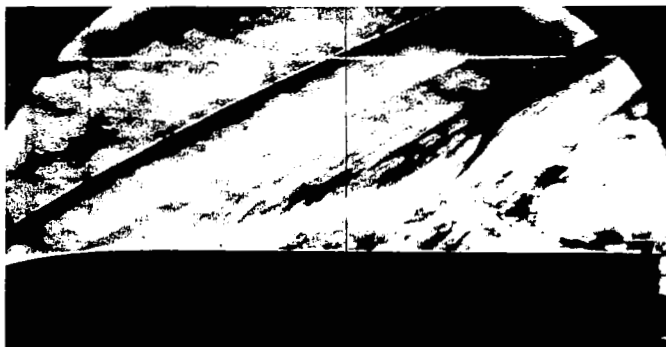
(b) $M_\infty = 4.5$.

Figure 12.- Continued.

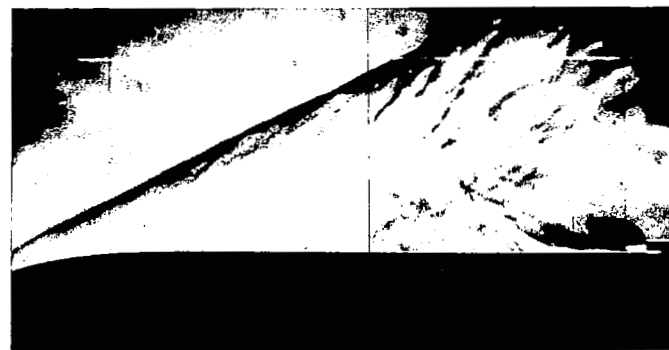


(c) $M_\infty = 6.0$.

Figure 12.- Concluded.



$M_j = 2.20$

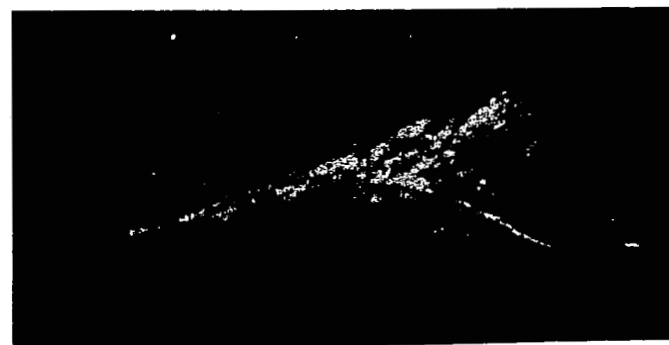


$M_j = 2.20$



$M_j = 3.68$

(a) $M_\infty = 3.0$.

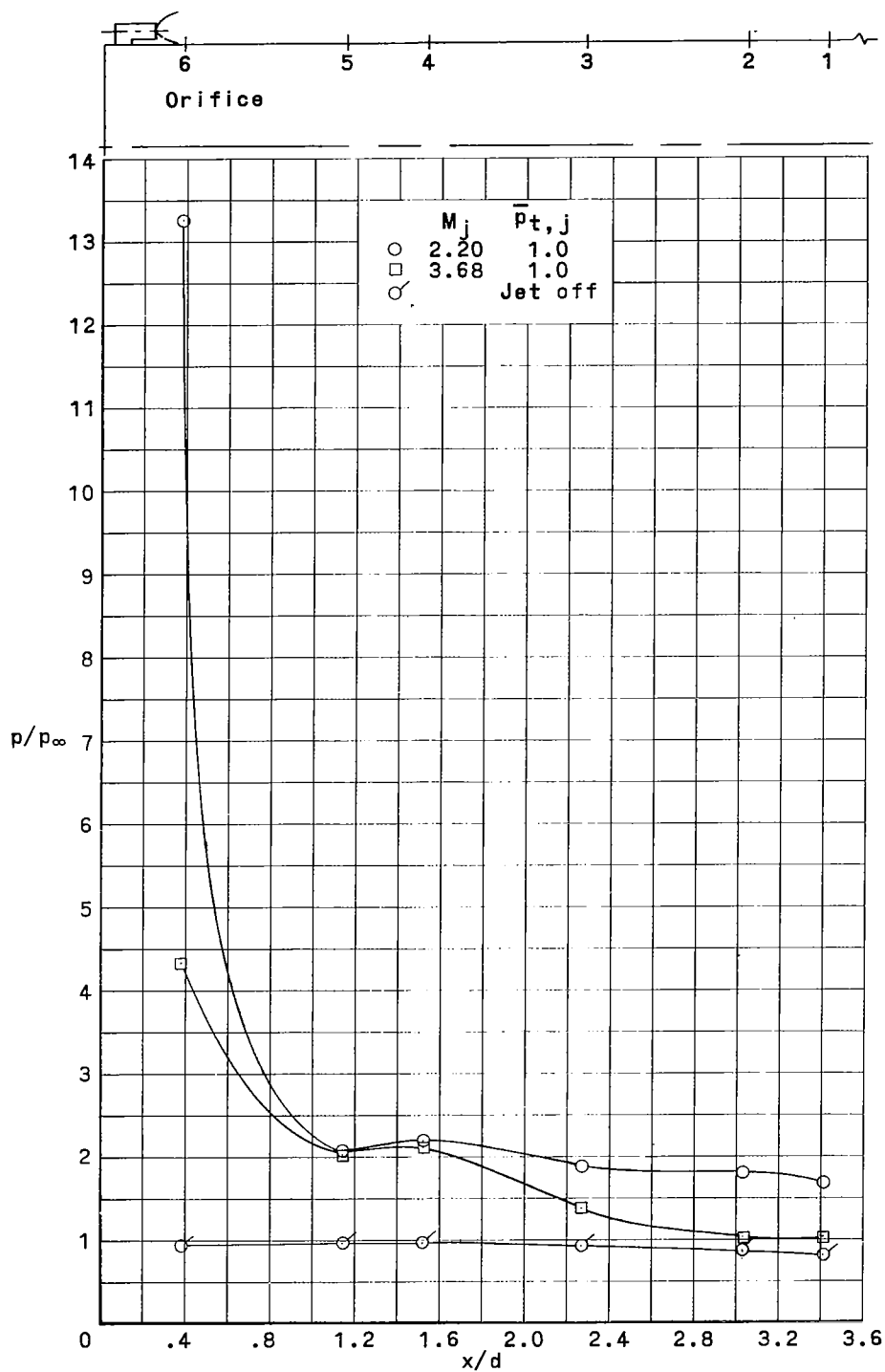


$M_j = 3.68$

(b) $M_\infty = 4.5$.

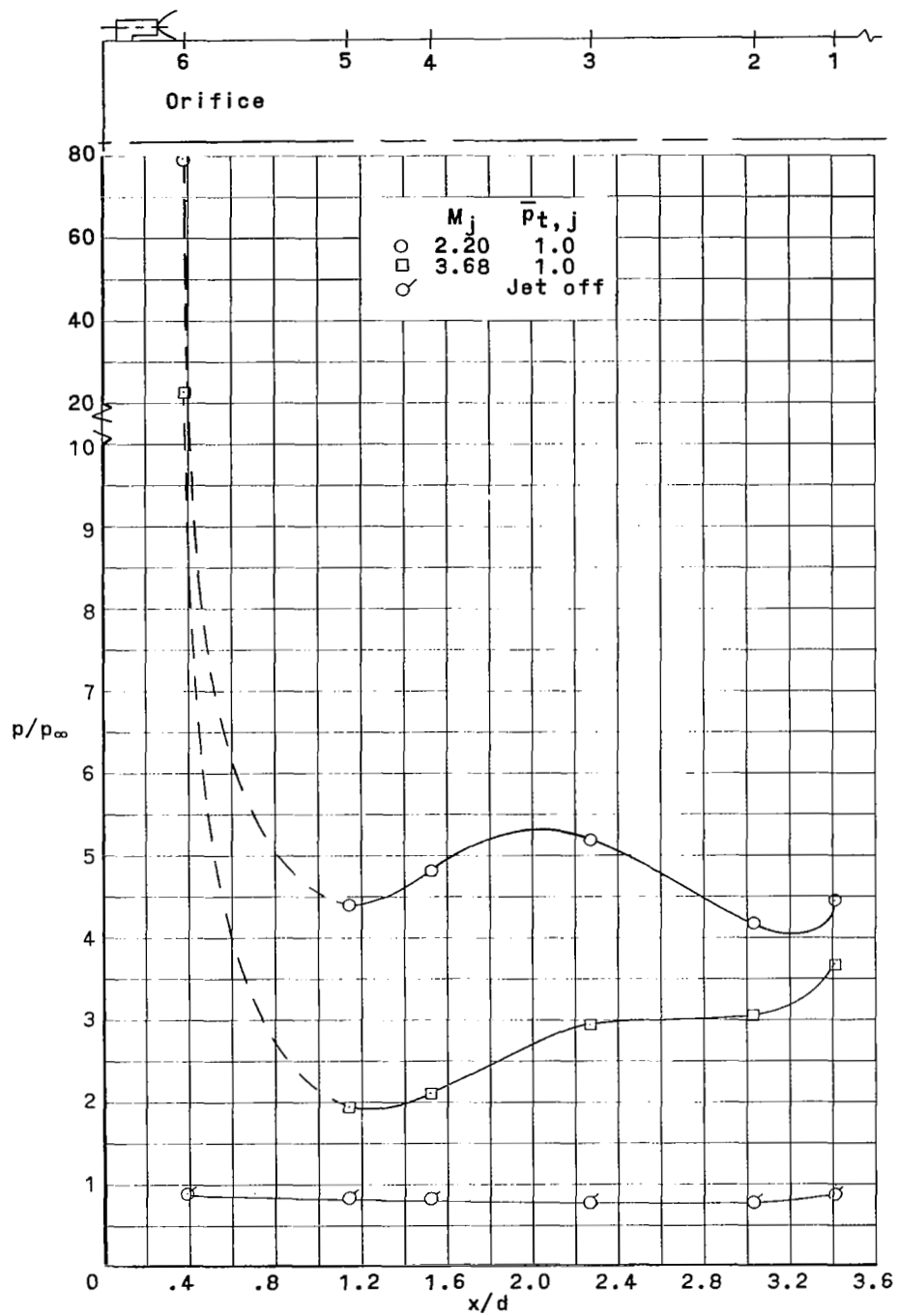
L-70-8019

Figure 13.- Effect of nozzle characteristics on the flow field for reference jet pressure. Ogive forebody; short centerbody; all four nozzles firing.



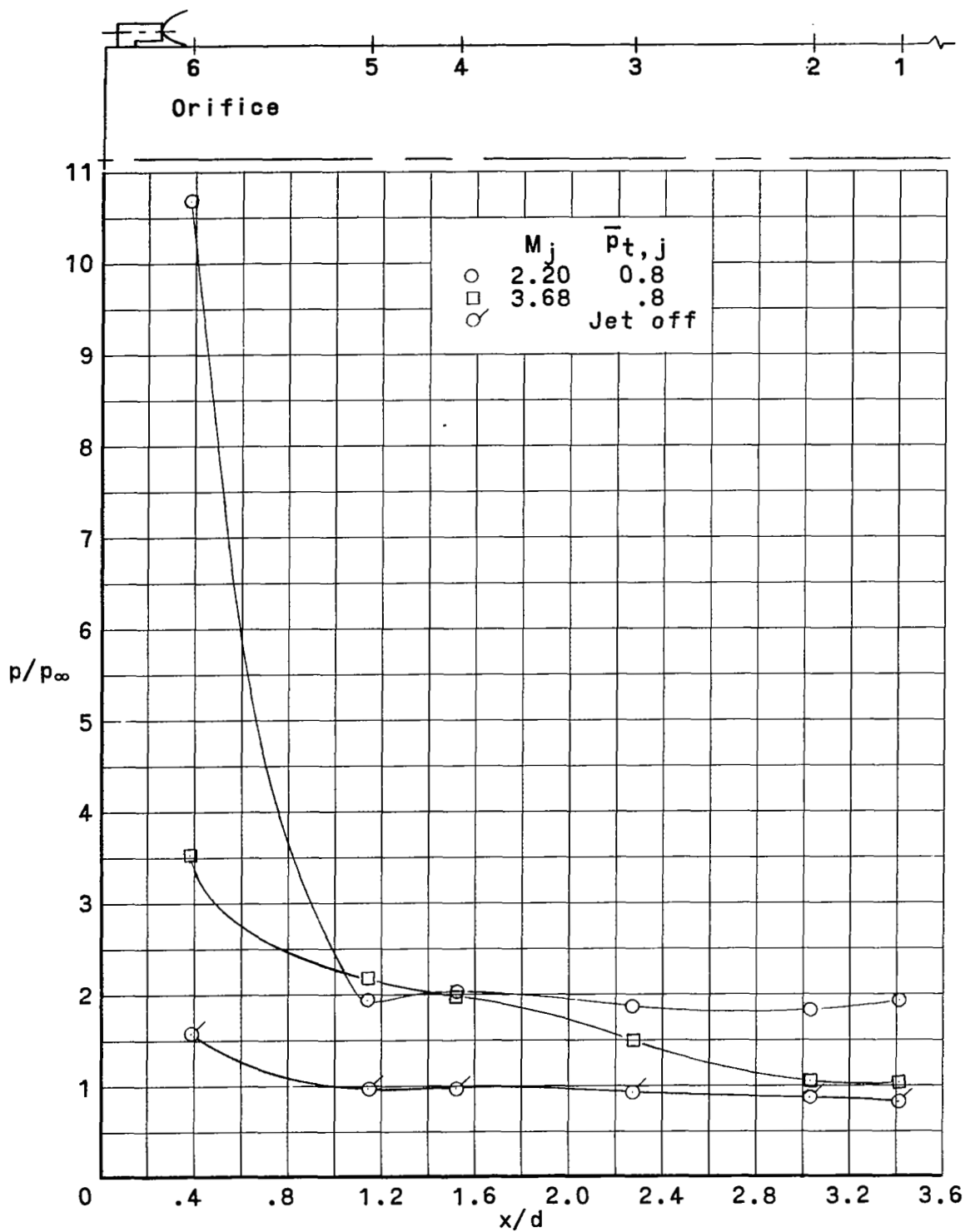
(a) $M_\infty = 3.0$.

Figure 14.- Effect of nozzle characteristics on the surface pressure distribution for reference jet pressure. Jet-off data included; ogive forebody; short centerbody; all four nozzles firing.



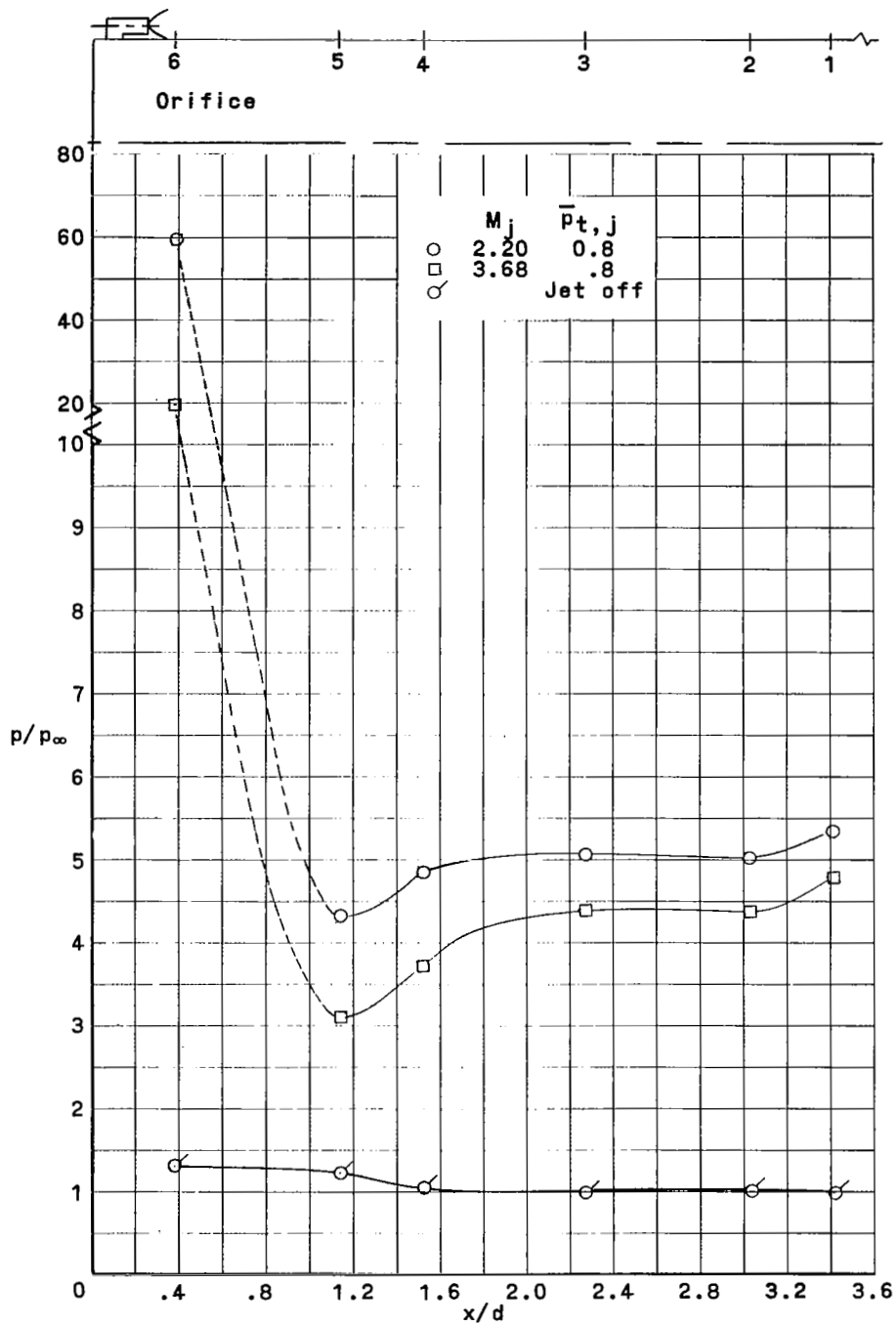
(b) $M_\infty = 4.5$.

Figure 14.- Concluded.



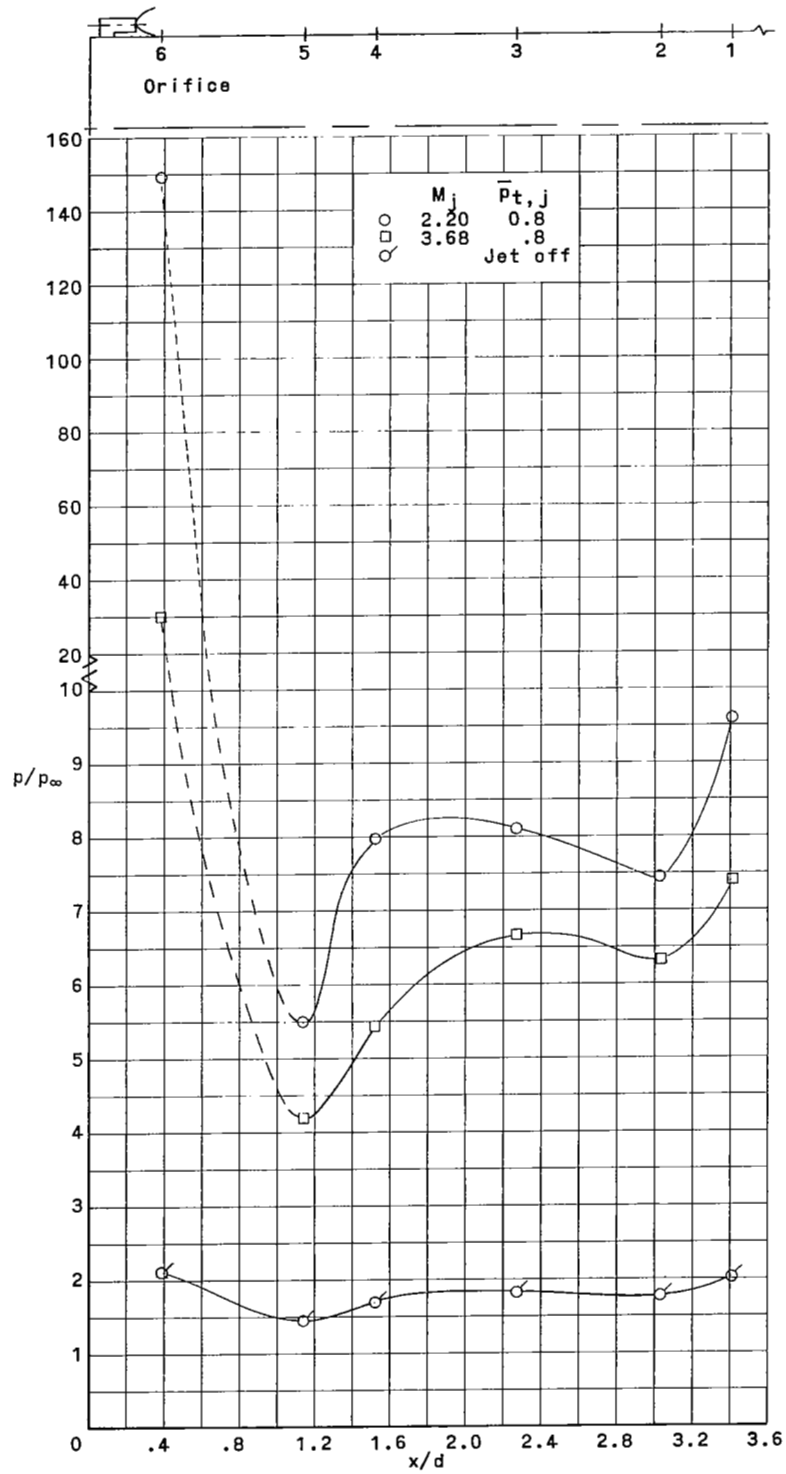
(a) $M_\infty = 3.0$.

Figure 15.- Effect of nozzle characteristics on the surface pressure distribution for 0.8 of the reference jet pressure. Jet-off data included; 30° cone forebody; short centerbody; all four nozzles firing.



(b) $M_\infty = 4.5$.

Figure 15.- Continued.

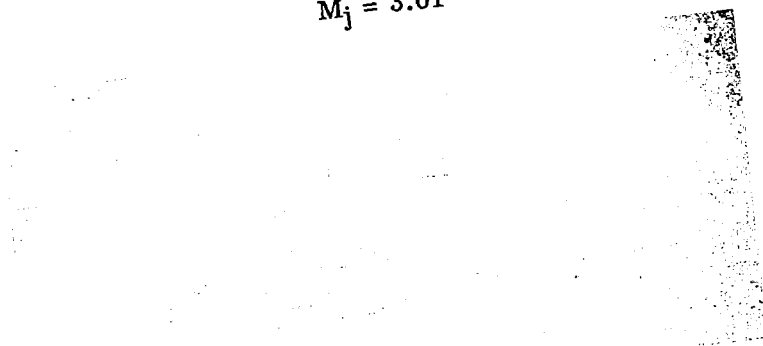


(c) $M_\infty = 6.0$.

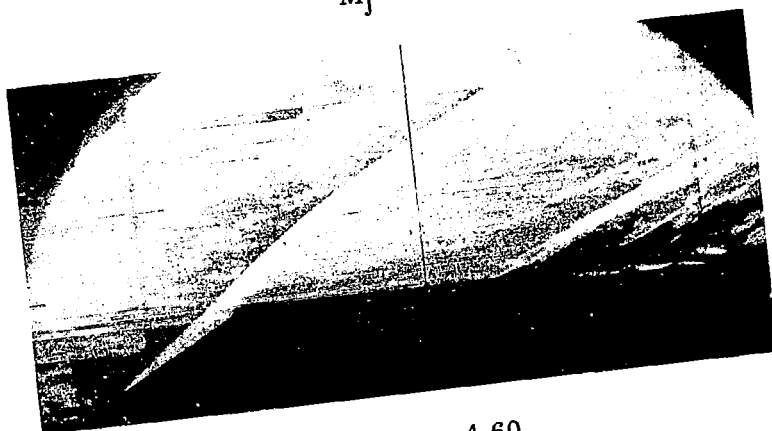
Figure 15.- Concluded.



$M_j = 3.01$



$M_j = 3.68$

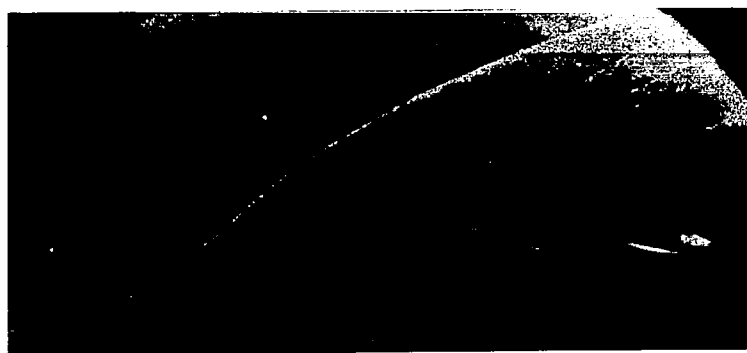


$M_j = 4.60$

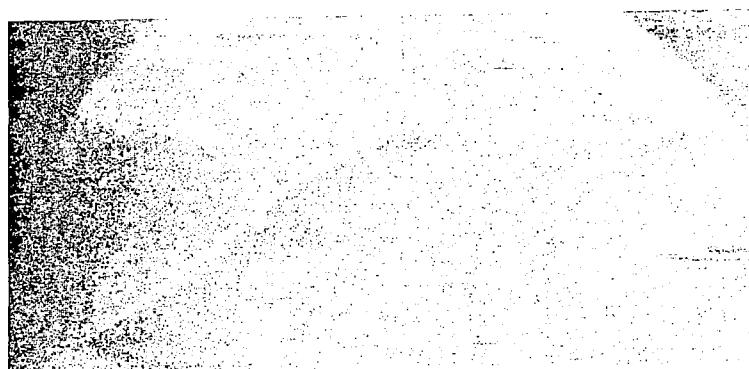
L-70-8020

(a) $M_\infty = 3.0$.

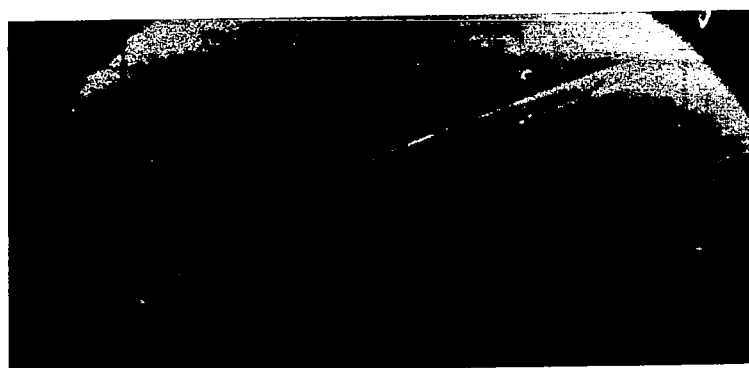
Figure 16.- Effect of nozzle characteristics on the flow field for reference jet pressure. 30° cone forebody; short centerbody; nozzle 1 firing.



$M_j = 3.01$



$M_j = 3.68$

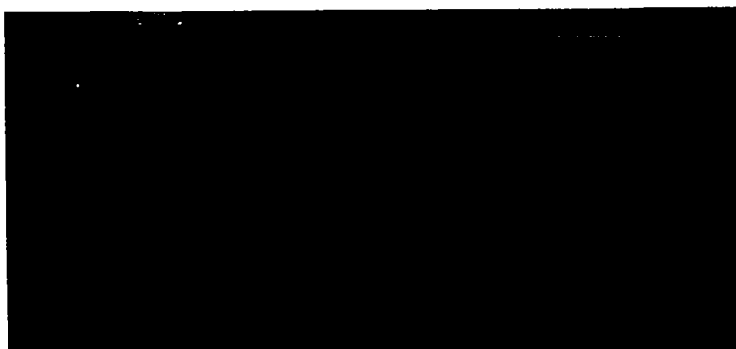


$M_j = 4.60$

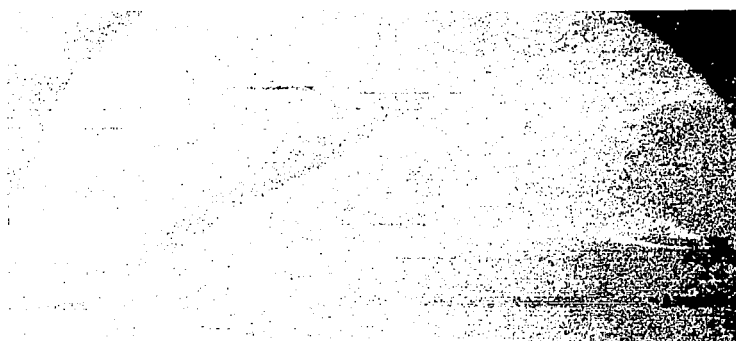
L-70-8021

(b) $M_\infty = 4.5.$

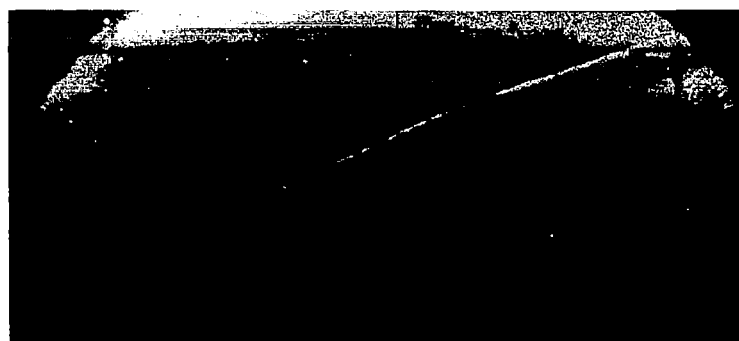
Figure 16.- Continued.



$$M_j = 3.01$$



$$M_j = 3.68$$

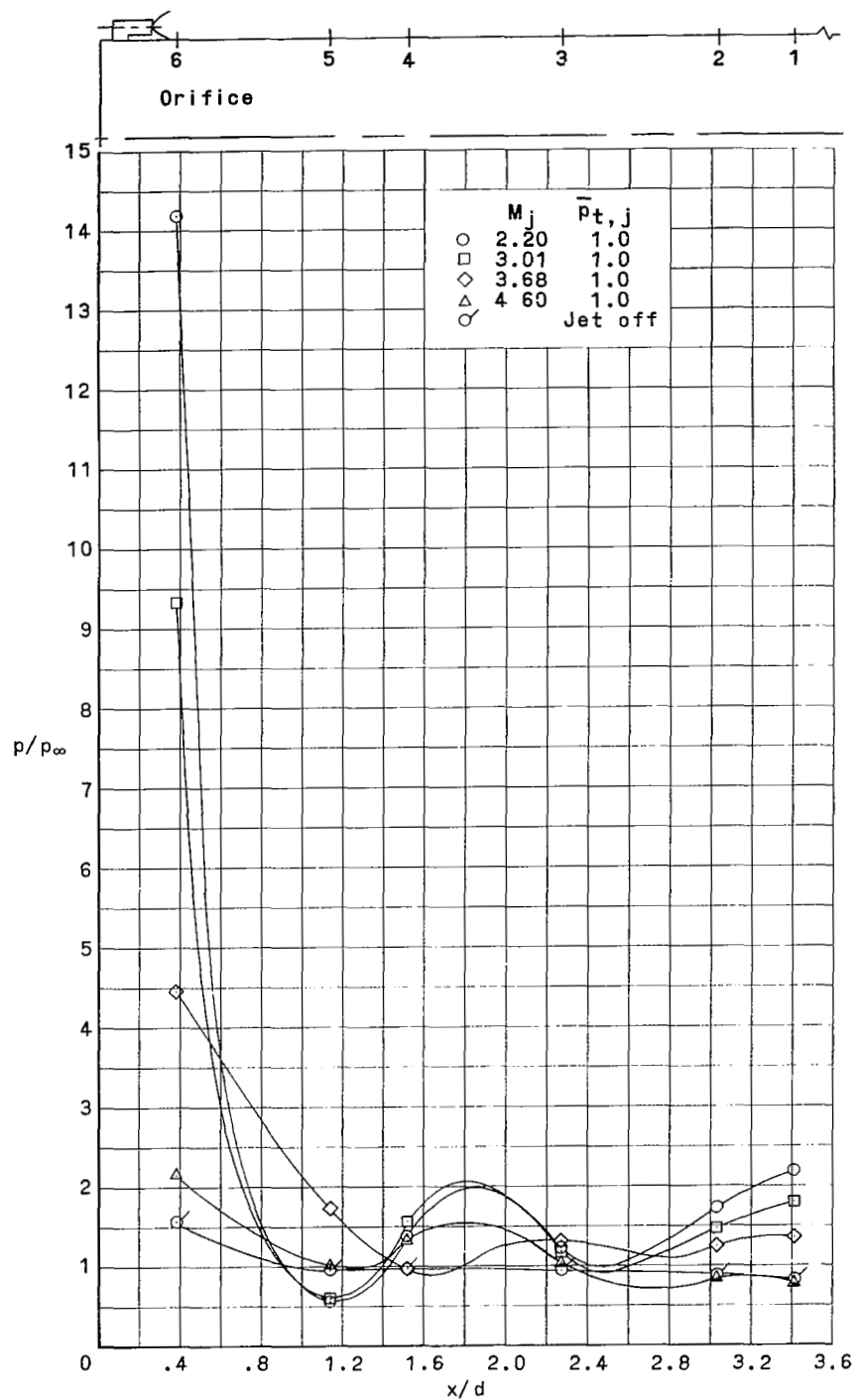


$$M_j = 4.60$$

L-70-8022

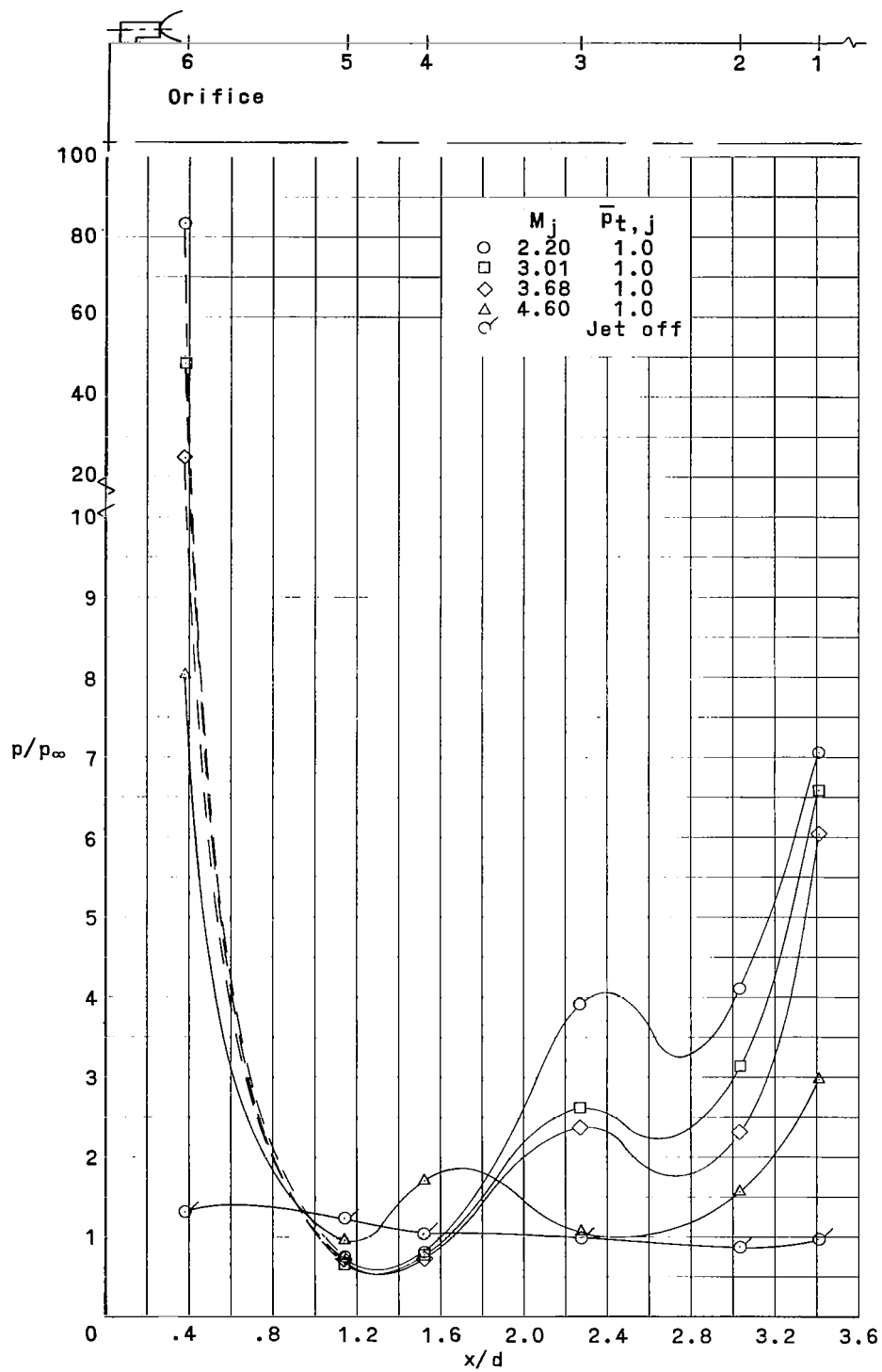
(c) $M_\infty = 6.0$.

Figure 16.- Concluded.



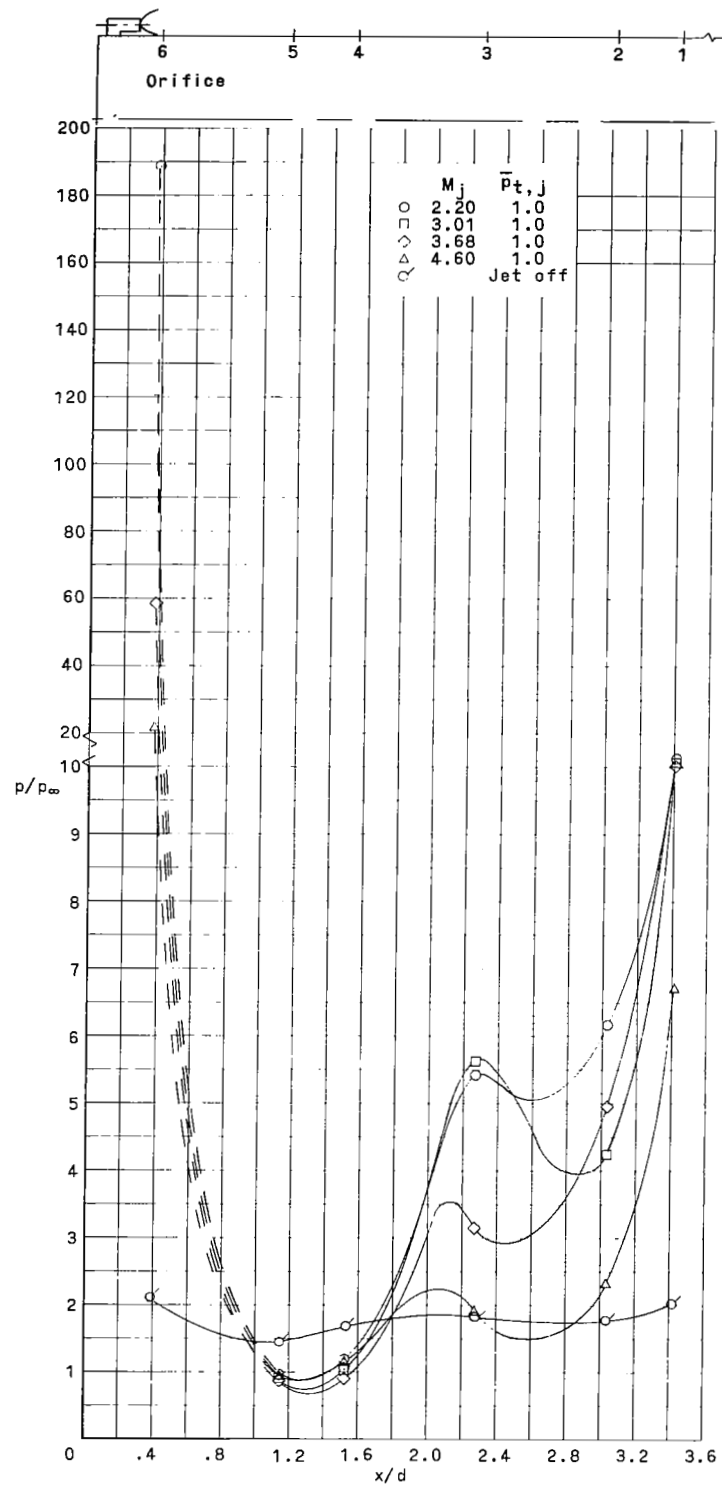
(a) $M_\infty = 3.0$.

Figure 17.- Effect of nozzle characteristics on the surface pressure distribution for reference jet pressure. Jet-off data included; 30° cone forebody; short center-body; nozzle 1 firing.



(b) $M_\infty = 4.5$.

Figure 17.- Continued.



(c) $M_\infty = 6.0$.

Figure 17.- Concluded.

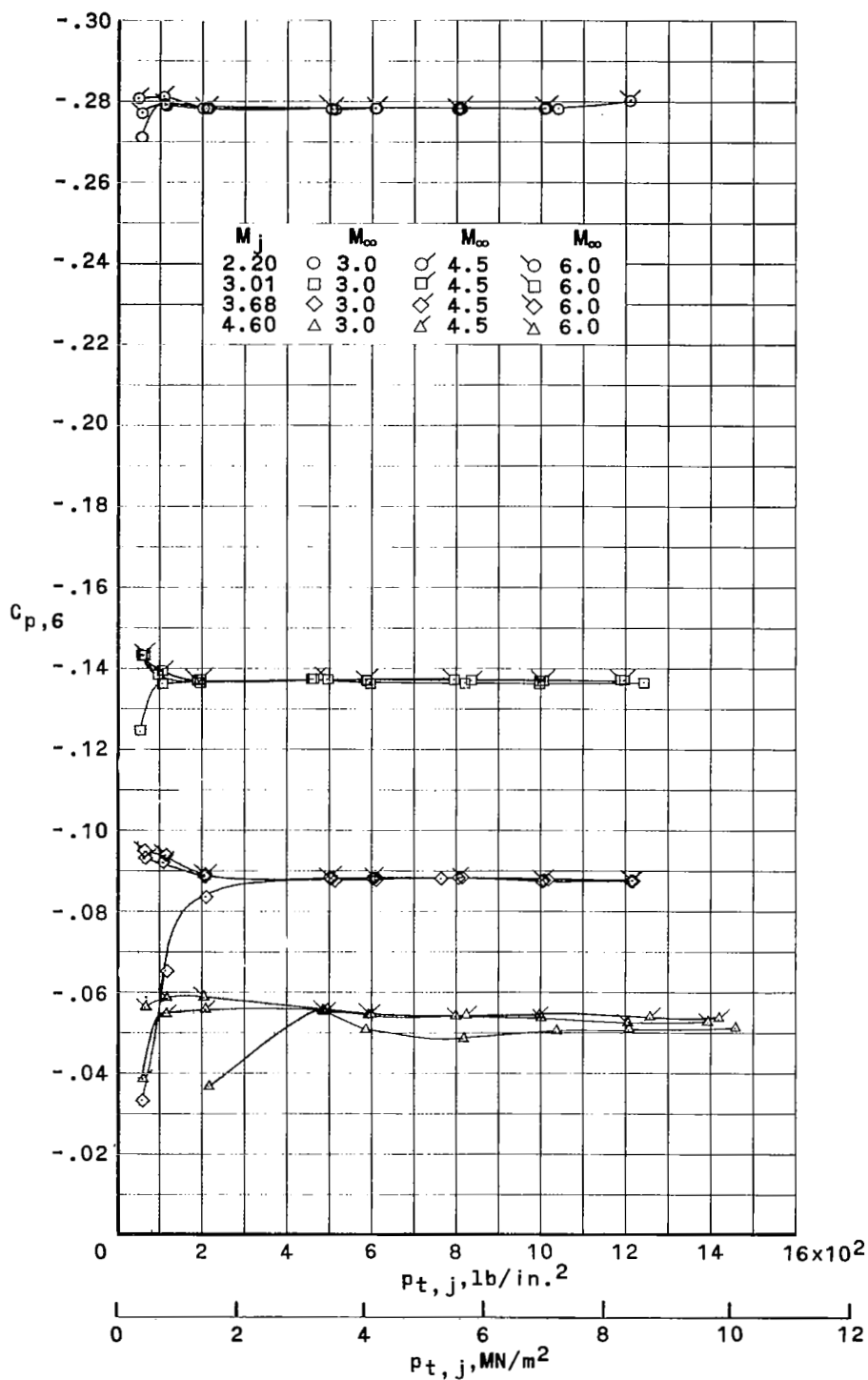


Figure 18.- Independence of $C_{p,6}$ from variations with M_∞ and $p_{t,j}$ for various values of M_j .

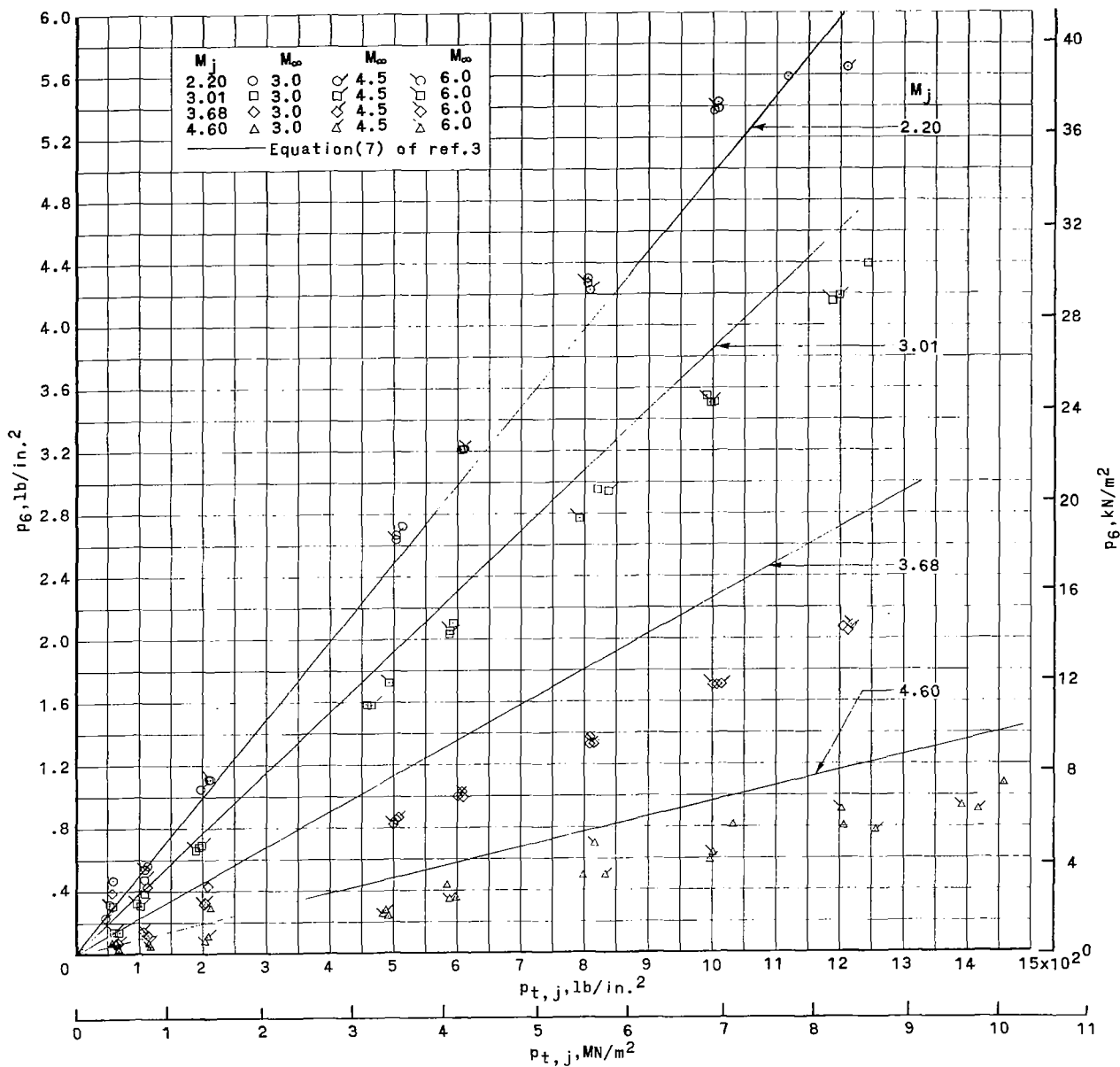


Figure 19.- Comparison of orifice 6 pressure data for 30° cone forebody, short centerbody, nozzle 1 firing with equation (7) of reference 3.

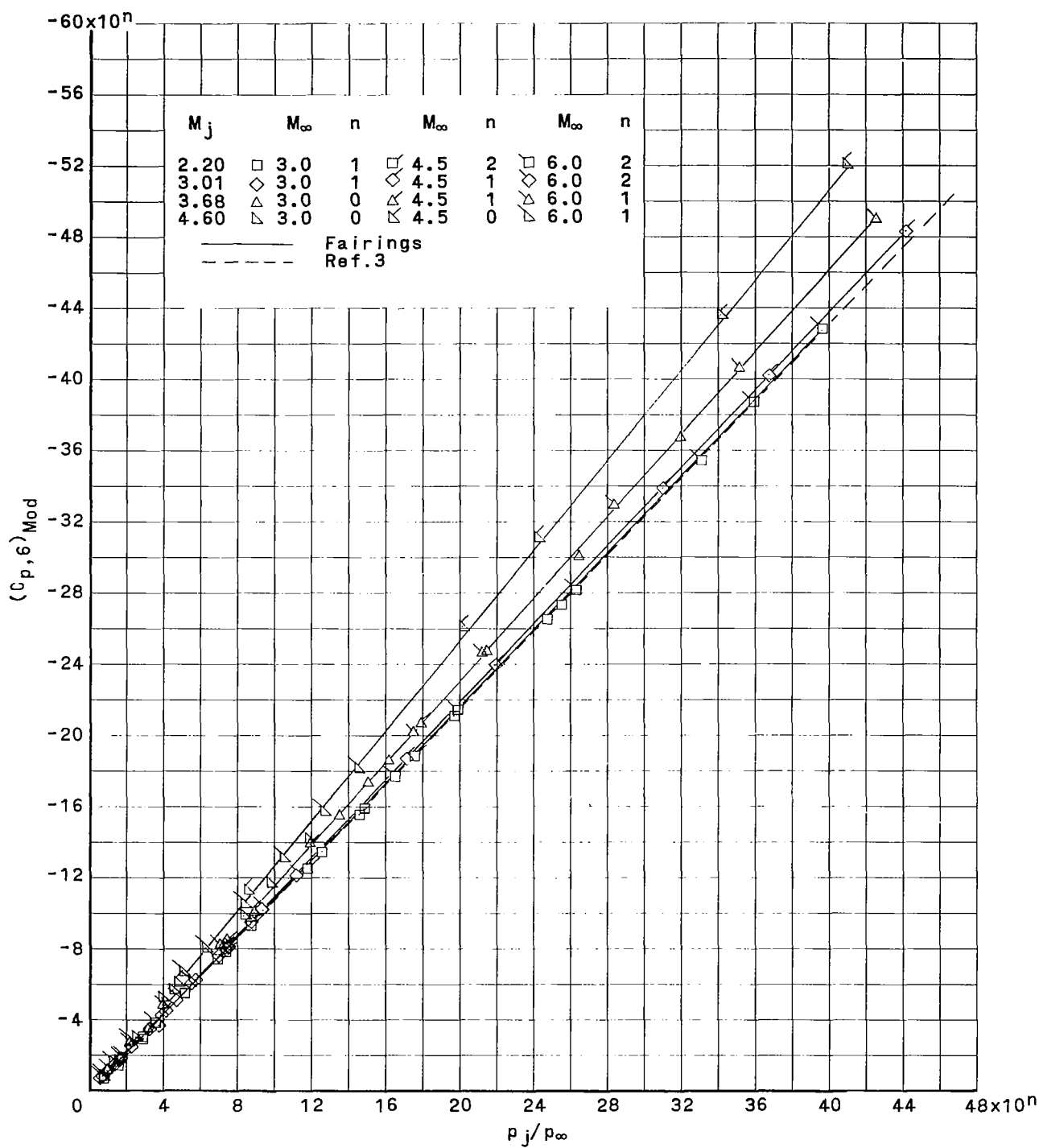


Figure 20.- Variation of modified pressure coefficient with p_j/p_∞ .